

Ejecta Width and Magnetization Reflected in Gamma-Ray Burst Early Afterglows: Implication for Reverse Shock Component and Shallow Decay Phase

Yo Kusafuka,^{1*} Katsuaki Asano¹

¹*Institute for Cosmic Ray Research, The University of Tokyo, 5-1-5 Kashiwanoha, Kashiwa, Chiba 277-8582, Japan*

Accepted XXX. Received YYY; in original form ZZZ

ABSTRACT

To study the ejecta property dependence of the gamma-ray burst (GRB) afterglow, we carry out spherically symmetrical one-dimensional special relativistic magneto-hydrodynamic simulations of magnetized outflows with an adaptive mesh refinement method. The Lorentz factor evolutions of forward and reverse shocks induced by the interaction between magnetized ejecta and an ambient medium are investigated for a wide range of magnetization and width of the ejecta. The forward shock evolution is described by the magnetic acceleration, coasting, transition, and self-similar deceleration phases. According to our simulation results, we numerically calculate the corresponding radiation. Based on our numerical results, to model afterglow light curves in general cases, we construct semi-analytical formulae for the Lorentz factor evolutions. The magnetization and ejecta width dependence are clearly seen in the reverse shock light curves. The transition phase with a reasonable ejecta width can reproduce the shallow decay phase in the observed GRB afterglow. The inverse Compton emission in the magnetic acceleration phase can be responsible for the very steep rise of the early TeV emission in GRB221009A.

Key words: MHD – relativistic process – ISM: jets and outflows – gamma-ray burst: general

1 INTRODUCTION

Gamma-ray bursts (GRBs) are the most luminous explosions in the Universe. Their enormous energy is promptly released within a few seconds to minutes, followed by a gradually fading afterglow radiation. The energy source of GRBs is thought to be the relativistic jets from compact remnants of the hypernovae or binary neutron star mergers. Dissipation of the energy through collision of the jet with interstellar mediums (ISM) or stellar winds causes multi-wavelength radiation. This external shock model can explain GRB afterglows (Rees & Meszaros 1992; Sari & Piran 1995; Mészáros & Rees 1997). While the analytical formulae by Sari et al. (1998) have been frequently adopted for the afterglow lightcurves, several numerical treatments obtained with hydrodynamical simulations (e.g. van Eerten et al. 2012; Ryan et al. 2020; Aksulu et al. 2020; Ayache et al. 2022) or the evolution of the electron energy distribution (e.g. Fukushima et al. 2017; Asano et al. 2020) have been also used to constrain the macroscopic and microscopic parameters. However, the ~40% (Evans et al. 2009; Li et al. 2018) of early X-ray afterglow lightcurves show shallower decay (Nousek et al. 2006; Liang et al. 2007) than what the standard model predicts. While the energy injection model (Zhang et al. 2006) has been considered for the shallow decay phase observed in the early afterglows, the chromatic break of optical lightcurves is hard to be explained (e.g. Fan & Piran 2006; Panaitescu et al. 2006; Rykoff et al. 2009). This may require another emission component such as emission from the reverse shock prop-

agating the ejecta (e.g. Perley et al. 2014; Japelj et al. 2014; Fraija et al. 2019; Gupta et al. 2021).

Launching mechanisms of relativistic jets are still debated, but extracting the rotation energy of a compact object by a global magnetic field may be the most promising process (Blandford & Znajek 1977). The magnetic launching mechanism generally produces magnetically dominated jets. Some simulations confirm that magnetically dominated outflows of $\sigma \gg 1$ can be launched through the magnetic process (Porth et al. 2019; Gottlieb et al. 2022), where σ is the magnetization parameter defined as the ratio of the Poynting flux to the enthalpy flux. Observationally, optical flashes probably originated from the reverse shock suggest that the jet is mildly or strongly magnetized (Fan et al. 2002; Wei et al. 2006; Roming et al. 2006; Racusin et al. 2008; Jin et al. 2013; Zhang et al. 2015; Huang et al. 2016). Polarization measurements of prompt emission also favor magnetized origin of jets (Gupta et al. 2022; Chattopadhyay et al. 2022; Veres et al. 2024), but a spectro-polarimetric analysis of GRB 160325A and GRB 160802A suggests a matter-dominated jet with marginal magnetization (Gupta et al. 2024). High polarization degrees of ~10% found in some GRB afterglows indicate the existence of the large scale ordered magnetic field (Bersier et al. 2003; Steele et al. 2009). For the brightest-of-all-time (BOAT) (LHAASO Collaboration et al. 2023), ultra-long duration (Ren et al. 2024) GRB 221009A, Yang et al. (2023); Zhang et al. (2024) claim the magnetic dominance at the dissipation radius.

The energy dissipation of jets can also occur inside themselves due to their variability. This internal shock model is often used to explain the prompt emission of GRBs and blazar flares (Rees 1978; Rees & Meszaros 1994; Kobayashi et al. 1997; Daigne & Mochkovitch 1998).

* E-mail: kusafuka@icrr.u-tokyo.ac.jp

Motivated by the Imaging X-ray Polarimetry Explorer (Weisskopf et al. 2022) observations for Mrk 501 (Di Gesu et al. 2022) and Mrk 421 (Liodakis et al. 2022), our previous study, Kusafuka et al. (2023) demonstrates the efficient magnetic energy dissipation by internal shock process. Magnetic pressure expansion converts the magnetic energy into the kinetic energy of the intermittent ejecta, which is then dissipated into the thermal energy by the shock waves. The dissipation efficiency is almost 10%, which is comparable to the reported radiative efficiency of GRBs and Blazars (Nemmen et al. 2012). However, this in turn suggests that the rest of the $\sim 90\%$ magnetic energy has remained in the region of the ejecta with $\sigma \gg 1$. Thus, magnetically dominated ejecta in the afterglow phase are naturally expected.

Even after the prompt emission, the ejecta can be accelerated by their remaining magnetic energy (Kusafuka et al. 2023). This late-phase magnetic acceleration is the same mechanism as the impulsive acceleration (Granot et al. 2011; Komissarov 2012). Some numerical simulations show the transition phase from the coasting phase to the self-similar deceleration phase so-called the Blandford-McKee solution (Blandford & McKee 1976). This intermediate phase is due to the initial finite radial width of the ejecta (Kobayashi & Sari 2000; Mimica et al. 2009; Kusafuka et al. 2023). This gradual evolution affects the temporal behaviour of the emission, but the analytical treatment for that phase is difficult (Gao et al. 2013). The dynamics of the forward and reverse shocks in this phase may be also affected by the magnetization, which has not been well studied especially for $\sigma \gg 1$.

In this paper, we study the effects of the initial magnetization and the radial width of the ejecta on the dynamics of the forward and reverse shocks by performing one-dimensional (1D) special relativistic magneto-hydrodynamical (SRMHD) simulations. We especially focus on the behaviour of the early afterglow emission including the reverse shock component and shallow decay phase. The paper is organised as follows. In Section 2, we describe the numerical method for the simulation of relativistic outflows and afterglow radiation. In Section 3, we show the results of forward shock radiation by interacting between magnetized ejecta and an ambient medium. In Section 4, we show the results of reverse shock radiation. In Section 5, we provide a semi-analytic model of our simulation results. In Section 6, we discuss the observational implications of our results for GRB early afterglow. The conclusion is summarised in Section 7.

Throughout the paper, we adopt the flat Λ CDM cosmology with the parameters from Planck Collaboration et al. (2020), where $H_0 = 67.66$ km/s/Mpc, $\Omega_b = 0.0490$, $\Omega_m = 0.3111$, and $\Omega_\Lambda = 0.6889$. We assume the source is located at $z = 1.0$ or $d_L = 2.1 \times 10^{28}$ cm, but neglecting the extra-galactic background light (EBL) absorption for simplicity. In most cases, the very high-energy gamma-ray community provides de-absorbed spectra adopting an EBL model in their observation papers.

2 SIMULATION METHOD

2.1 Fluid Dynamics

In this paper, we consider magnetically-dominated relativistic ejecta (magnetic bullets) launched from a central engine. To investigate the afterglow radiation from magnetic bullets via interaction with an ambient medium, we carry out 1D SRMHD simulations assuming spherically symmetric geometry. 1D simulations are free from fluid instabilities. In a realistic system, the Rayleigh–Taylor instability may affect on a contact discontinuity to mix the forward and

reverse shocked regions. The Kelvin–Helmholtz instability may also contribute to mixing an ejecta with a surrounding medium. For magnetized ejecta, the Kink instability can induce magnetic reconnection to reduce magnetization. We neglect the effects of such instabilities in this paper. We also neglect a lateral structure and a lateral spreading effect of the ejecta, which can affect especially late phase afterglows (Rhoads 1999; van Eerten & MacFadyen 2012; Duffell & Laskar 2018; Ryan et al. 2020).

Our simulation method is updated from the previous version in Kusafuka et al. (2023). We improve the spatial and time interpolation of variables to achieve a much higher resolution than that in our previous simulations, whose scheme has the 2nd-order interpolation. In addition, we adopt a moving window technique (Mimica et al. 2004) to reduce the computational cost drastically. The details are given in Section 2.1.2.

2.1.1 Fundamental equations

We only consider the radial component for the fluid velocity $\mathbf{v} = (v, 0, 0)$ and the θ -component for the magnetic field $\mathbf{B} = (0, B, 0)$, which are measured at the rest frame of the ambient medium. On the other hand, the mass density ρ , gas pressure p , and energy density ϵ are measured at the fluid rest frame. The equation of state is

$$\epsilon = \frac{p}{\hat{\gamma} - 1} + \rho c^2, \quad (1)$$

where $\hat{\gamma}$ is the adiabatic index. As suggested by Mignone et al. (2005) taking the equal sign in Taub’s inequality (Taub 1948), the equation of state is approximately expressed as $p = (\epsilon^2 - \rho^2 c^4)/(3\epsilon)$ with correct cold and relativistic asymptotic values (Mignone & McKinney 2007). Combining with Eq. (1), we can derive the adiabatic index as

$$\hat{\gamma} = 1 + \frac{\epsilon + \rho c^2}{3\epsilon}. \quad (2)$$

The mass, energy, momentum conservation laws, and the induction equation are described as (e.g. Mimica et al. 2009)

$$\frac{1}{c} \frac{\partial \rho \Gamma}{\partial t} + \frac{1}{r^2} \frac{\partial}{\partial r} (r^2 \rho \Gamma \beta) = 0, \quad (3)$$

$$\begin{aligned} \frac{1}{c} \frac{\partial}{\partial t} \left[\left(\epsilon + p + \frac{B^2}{4\pi\Gamma^2} \right) \Gamma^2 - p - \frac{B^2}{8\pi\Gamma^2} \right] \\ + \frac{1}{r^2} \frac{\partial}{\partial r} \left(r^2 \left[\left(\epsilon + p + \frac{B^2}{4\pi\Gamma^2} \right) \Gamma^2 \beta \right] \right) = 0, \end{aligned} \quad (4)$$

$$\begin{aligned} \frac{1}{c} \frac{\partial}{\partial t} \left[\left(\epsilon + p + \frac{B^2}{4\pi\Gamma^2} \right) \Gamma^2 \beta \right] \\ + \frac{1}{r^2} \frac{\partial}{\partial r} \left(r^2 \left[\left(\epsilon + p + \frac{B^2}{4\pi\Gamma^2} \right) \Gamma^2 \beta^2 + p + \frac{B^2}{8\pi\Gamma^2} \right] \right) = \frac{2p}{r}, \end{aligned} \quad (5)$$

$$\frac{1}{c} \frac{\partial B}{\partial t} + \frac{1}{r} \frac{\partial}{\partial r} (r\beta B) = 0, \quad (6)$$

respectively, where $\beta = v/c$ is the fluid velocity normalised by the speed of light, and $\Gamma = 1/\sqrt{1-\beta^2}$ is the Lorentz factor of the fluid. For the parameterisation in our simulations, we define the magnetization parameter σ as

$$\sigma \equiv \frac{B^2}{4\pi(\epsilon + p)\Gamma^2}. \quad (7)$$

2.1.2 Numerical technique

For the spatial interpolation of variables, we adopt the 7th-order MP7 scheme (Suresh & Huynh 1997). For the time interpolation of variables, we use the 3rd-order Strong Stability Preserved Runge-Kutta (Gottlieb & Shu 1998) and set the CFL number around 0.3. We use the minmod function as a flux limiter (Roe 1986), and compute numerical flux by approximate Riemann solver, the CENTRAL scheme (Kurganov & Tadmor 2000), or so-called Rusanov scheme (Rusanov 1962). For the primitive recovery, we use the Newton-Raphson method (Mignone & Bodo 2006). We implement the adaptive mesh refinement (Berger & Olinger 1984, AMR) to obtain a higher resolution around discontinuities. To reduce enormous computational costs, we use a moving window technique (Mimica et al. 2004) to follow only around shock waves in the ejecta. To minimise artificial boundary effects, we set the box size to 20 times larger than the initial width of the ejecta.

In high σ cases, an insufficient resolution will affect the reverse shock dynamics, making the shock crossing time longer (Kusafuka et al. 2023). We have confirmed that our resolution is enough to capture the reverse shock dynamics accurately by our means of resolution study.

2.1.3 Initial setup

The simulation window is in the ambient medium rest frame. For the ambient medium, we assume that the magnetic field and the number density are homogeneous and set as $1 \mu\text{G}$ and $n_0 = 1 \text{ cm}^{-3}$, respectively. The magnetic field configuration in a typical GRB environment may not be homogeneous, but the field in the ambient medium is so weak that the forward shock dynamics is not affected. In addition, as usually assumed, we amplify the magnetic field in the forward shocked region adopting the microscopic parameter ϵ_B to calculate the emission property. The temperature is also fixed as a non-relativistic temperature of 1 MeV to stabilize the simulations, but it is sufficiently cold not to affect the evolution of the dynamics.

The initial magnetic field of the ejecta is written as

$$B = \sqrt{4\pi(\epsilon + p)\Gamma_0^2\sigma_0}, \quad (8)$$

where σ_0 and $\Gamma_0 = 10$ are the initial magnetization and the Lorentz factor of the ejecta, respectively. We define the deceleration radius R_{dec} as (Sari & Piran 1995)

$$R_{\text{dec}} = \left(\frac{3E_0}{4\pi n_0 m_p c^2 \Gamma_0^2} \right)^{1/3}. \quad (9)$$

The inner edge of the ejecta is initially set at $R_0 = 0.1R_{\text{dec}}$. We consider two cases for the initial width of the ejecta: thick shell case $\Delta_0 = R_{\text{dec}}/\Gamma_0^2$ and thin shell case $\Delta_0 = R_0/\Gamma_0^2$. We assume that the ejecta has initially homogeneous magnetization σ_0 , temperature $T_0 = 100 \text{ MeV}$, and Lorentz factor Γ_0 , but the mass density follows as $\rho = \rho_0(r/R_0)^{-2}$ in the initial condition. The initial energy of the ejecta is set to be $E_0 = 10^{50} \text{ erg}$, from which the normalisation of the mass density ρ_0 can be calculated. The deceleration radius R_{dec} is $5.4 \times 10^{16} \text{ cm}$ for $E_0 = 10^{50} \text{ erg}$, $\Gamma_0 = 10$, and $n_0 = 1 \text{ cm}^{-3}$.

The simulation window size is $20\Delta_0$. The outer boundary is a moving boundary, where a simulation window moves one cell outer when the forward shock is at the 50 cells before the outer boundary. The inner boundary is set to be an injection boundary, where we inject a plasma with a significantly low luminosity with $\Gamma = 2$ continuously to avoid a numerical floor. The initial inner boundary is at 500 static cells before the position of the rear edge of the ejecta. The initial

width of the ejecta is resolved by 10^3 static cells and effectively almost 10^4 static cells.

2.2 Radiation

Based on our simulation results of the dynamics of shock waves, we calculate radiation from the shocks as a post-process with the one-zone approximation. From the simulation results, we detect the forward and reverse shock radii R . Using the physical quantities just behind the shocks, the density n , internal energy density ϵ , Lorentz factor Γ , and magnetic field $B' = B/\Gamma$, we calculate radiation from the two shock fronts. We consider two emission mechanisms: synchrotron radiation and synchrotron self-Compton (SSC) emission. In addition, we take into account two absorption processes: synchrotron self-absorption (SSA) and $\gamma\gamma$ annihilation. Some hadronic emissions such as proton synchrotron and pion production might be dominant in the early phase afterglow, but we leave these effects for future studies.

2.2.1 Non-thermal particle spectra

At or around shock waves, charged particles are accelerated through diffusive shock acceleration (DSA) (Blandford & Ostriker 1978; Bell 1978), magnetic reconnection (Sironi & Spitkovsky 2011; Sironi et al. 2015), or turbulent acceleration (Asano & Terasawa 2009; Asano et al. 2014). We assume that electrons are injected with a single power law distribution as (Sari et al. 1998)

$$n_{\text{inj}}(\gamma) \propto \gamma^{-p}, \quad \gamma_m \leq \gamma \leq \gamma_M, \quad (10)$$

where $n_{\text{inj}}(\gamma)$ is the comoving spectral number density at injection as a function of the Lorentz factor γ of electrons. Non-relativistic DSA theory expects the spectral index becomes $p = 2.0$ in the strong shock limit (Blandford & Ostriker 1978; Bell 1978). However, in the case of relativistic shocks, the index becomes $p \sim 2.2$ in the same limit (Keshet & Waxman 2005). Thus, we set the spectral index p as a fixed value $p = 2.2$ for simplicity in this study. In general, the index may be larger than 2.2, making a radiation spectrum softer (Sari et al. 1998). The normalization of $n_{\text{inj}}(\gamma)$ and the minimum Lorentz factor γ_m are determined by assuming that all electrons behind the shock front are accelerated, and obtain an energy fraction $\epsilon_e (= 0.1$ in our simulations) to the internal energy density ϵ (Sari et al. 1998):

$$\gamma_m = 1 + \frac{p-2}{p-1} \frac{\epsilon_e \epsilon}{nm_e c^2}, \quad (11)$$

The maximum Lorentz factor is given by the balance of acceleration with the Bohm limit and synchrotron cooling, or the confinement condition (Hillas 1984):

$$\gamma_M = \min \left(\sqrt{\frac{6\pi e}{\sigma_T B'}}, \frac{eB'\Delta R}{m_e c^2} \right), \quad (12)$$

where σ_T is Thomson scattering cross section, e is the elementary charge, m_e is the electron mass. The shell width of the forward shock $\Delta R \equiv R_{\text{FS}}/(12\Gamma_{\text{FS}})$ is estimated from the simulation results of the forward shock radius R_{FS} and the Lorentz factor Γ_{FS} . The shell width of the reverse shock $\Delta R \equiv \Gamma_{\text{RS}}(R_{\text{CD}} - R_{\text{RS}})$ is estimated from the simulation results of the contact discontinuity radius R_{CD} , the reverse shock radius R_{RS} , and the Lorentz factor Γ_{RS} . For the forward shock emission, we assume that the magnetic field amplification is due to kinetic instabilities (e.g. Weibel instability). An energy fraction $\epsilon_B (= 0.01$ in our simulations) to the internal energy density ϵ can be

transferred to the generated turbulent magnetic field energy (Sari et al. 1998):

$$B' = \sqrt{8\pi\epsilon_B\epsilon}. \quad (13)$$

For the reverse shock emission, the magnetic field is adopted from the simulation date.

The spectra of these non-thermal particles are modified by radiative cooling. The continuity equation of electrons is

$$\frac{dn(\gamma)}{dt} + \frac{\partial}{\partial\gamma} \left(n(\gamma) \frac{d\gamma}{dt} \right) = Q, \quad (14)$$

where Q is the injection term estimated from Eq. (10). The radiative cooling function is given by

$$\frac{d\gamma}{dt} = -\frac{\sigma_T B'^2}{6\pi mc} \gamma^2 [1 + Y(\gamma)], \quad (15)$$

where Y is the Compton parameter defined as the ratio of SSC power and synchrotron power. Due to the Klein-Nishina effect, the Compton Y has energy dependence (Fan & Piran 2006)

$$Y(\gamma) = \frac{-1 + \sqrt{1 + 4\epsilon_{\text{rad}}\eta_{\text{KN}}\epsilon_e/\epsilon_B}}{2}, \quad (16)$$

where $\epsilon_{\text{rad}} = \min\left(1, (\gamma_m/\gamma_c)^{(p-2)}\right)$ is the fraction of radiated electron energy (Sari & Esin 2001), and η_{KN} is Klein-Nishina correction factor. For fast cooling case ($\gamma_c < \gamma_m$),

$$\eta_{\text{KN}} = \begin{cases} 0 & \hat{\gamma} < \gamma_c \\ \frac{\hat{\gamma} - \gamma_c}{[(p-1)/(p-2)]\gamma_m - \gamma_c} & \gamma_c < \hat{\gamma} < \gamma_m \\ 1 - \frac{\gamma_m^{p-1}\hat{\gamma}^{2-p}}{(p-1)\gamma_m - (p-2)\gamma_c} & \gamma_m < \hat{\gamma} \end{cases}, \quad (17)$$

while for slow cooling case ($\gamma_m < \gamma_c$),

$$\eta_{\text{KN}} = \begin{cases} 0 & \hat{\gamma} < \gamma_m \\ \frac{\hat{\gamma}^{3-p} - \gamma_m^{3-p}}{[1/(p-2)]\gamma_c^{3-p} - \gamma_m^{3-p}} & \gamma_m < \hat{\gamma} < \gamma_c \\ 1 - \frac{(3-p)\gamma_c\hat{\gamma}^{2-p}}{\gamma_c^{3-p} - (p-2)\gamma_m^{3-p}} & \gamma_c < \hat{\gamma} \end{cases}, \quad (18)$$

where $\hat{\gamma} = \sqrt{4\pi m_e c \hat{\nu}' / (3eB')}$ and $\hat{\nu}'$ is given by $\gamma h \hat{\nu}' = \Gamma m_e c^2$ (Fan & Piran 2006; Ren et al. 2024).

We take the MHD snapshot in every 10^4 s, which is shorter than the dynamical timescale $R/(\Gamma c)$ at any time. This guarantees the particle distribution is steady in each snapshot, and then the corresponding particle spectra are analytically calculated from Eq. (14). For the fast cooling case ($\gamma_c < \gamma_m$) (Nakar et al. 2009; Wang et al. 2010),

$$n(\gamma) \propto \frac{1}{1+Y(\gamma)} \begin{cases} \gamma^{-2} & \gamma_c < \gamma < \gamma_m \\ \gamma^{-p-1} & \gamma_m < \gamma \end{cases}, \quad (19)$$

while for the slow cooling case ($\gamma_m < \gamma_c$),

$$n(\gamma) \propto \begin{cases} \gamma^{-p} & \gamma_m < \gamma < \gamma_c \\ \frac{1}{1+Y(\gamma)} \gamma^{-p-1} & \gamma_c < \gamma \end{cases}, \quad (20)$$

where the cooling break energy γ_c is determined by the balance of radiative cooling timescale and dynamical timescale:

$$\gamma_c = \frac{6\pi\Gamma m_e c^2}{\sigma_T B'^2 R (1+Y(\gamma_c))}. \quad (21)$$

2.2.2 Translation to the Observer Frame

Due to the relativistic Doppler effect, the observed frequency is boosted as

$$\nu_{\text{obs}} = \mathcal{D} \frac{\nu'}{1+z}, \quad (22)$$

where z is the cosmological redshift and \mathcal{D} is the Doppler factor:

$$\mathcal{D}(\theta) = \frac{1}{\Gamma(1 - \beta \cos \theta)}, \quad (23)$$

representing the angle between the line of sight and the direction of the fluid motion by θ .

We also consider the Equal Arrival Time Surface (EATS) for the observed radiation flux (Waxman 1997; Granot 2005). We define the observed time t_{obs} at which photons emitted from a position at (R, θ) arrive at the observer,

$$t_{\text{obs}} \equiv (1+z) \left[t - \frac{R(t) - R_0}{c} \cos \theta \right], \quad (24)$$

where t is measured at the engine rest frame. To compute the observed radiation flux, we should integrate over solid angle $d\Omega = 2\pi \sin \theta d\theta$. The relativistic beaming effect allows us to integrate within a small angle. In our calculation, the maximum angle for the integral is chosen as $\theta_0 = 3\Gamma^{-1}$.

2.2.3 Synchrotron radiation

To calculate the observed synchrotron flux F_ν , we first evaluate the comoving synchrotron emissivity $j'_{\text{syn},\nu'}$ as (Rybicki & Lightman 1986)

$$j'_{\text{syn},\nu'} = \frac{1}{4\pi} \int_{\gamma_m}^{\gamma_M} d\gamma n(\gamma) \frac{\sqrt{3}e^3 B' \sin \alpha}{m_e c^2} \mathcal{F} \left(\frac{\nu'}{\gamma'_0} \right), \quad (25)$$

where we use the averaged value of $\sin \alpha = \pi/4$, the typical synchrotron frequency $\nu'_0 = 3eB'\gamma_e^2/(4\pi m_e c)$, and the fitting formulae for calculating the non-dimensional function $\mathcal{F}(x)$ (Fouka & Ouichaoui 2013). Then, the isotropic-equivalent flux is written as

$$F_{\text{syn},\nu}(t_{\text{obs}}) = (1+z) \int \frac{R^2 d\Omega}{d_L^2} \mathcal{D}^3 \Delta R \frac{j'_{\text{syn},\nu'}}{\tau_{\text{SSA}}} (1 - \exp(-\tau_{\text{SSA}})), \quad (26)$$

where d_L is the luminosity distance, and $R^2 \Delta R$ is a function of t_{obs} and θ given by the EATS. The optical depth due to SSA $\tau_{\text{SSA}} = \alpha_\nu \Delta R$ is written with the absorption coefficient

$$\alpha_\nu = \frac{-1}{8\pi m_e \nu^2} \int d\gamma \frac{\sqrt{3}e^3 B \sin \alpha}{m_e c^2} \mathcal{F} \left(\frac{\nu}{\nu_0} \right) \gamma^2 \frac{\partial}{\partial\gamma} \left(\frac{n(\gamma)}{\gamma^2} \right). \quad (27)$$

2.2.4 Synchrotron self-Compton process

We calculate the comoving SSC emissivity $j'_{\text{SSC},\nu'}$ as (Fan et al. 2008)

$$j'_{\text{SSC},\nu'} = \frac{1}{4\pi} \int h\nu' n_{\text{ph}}(\gamma) n(\gamma) d\gamma, \quad (28)$$

where h is the Planck constant, and $n_{\text{ph}}(\gamma)$ is the scattered photon spectrum per electron.

$$n_{\text{ph}}(\gamma) = \int d\nu'_{\text{syn}} \frac{3\sigma_T c n_{\nu'_{\text{syn}}} F_{\text{KN}}(g, q)}{4\gamma^2 \nu'_{\text{syn}}}. \quad (29)$$

The typical frequency of a scattered photon is

$$\nu' = \frac{\gamma^2 \nu'_{\text{syn}}}{1+g}, \quad (30)$$

where g is the threshold for the Klein-Nishina effect defined by

$$g \equiv \frac{\gamma h \nu'_{\text{syn}}}{m_e c^2}. \quad (31)$$

The comoving synchrotron photon number density is written as

$$n_{\nu'_{\text{syn}}} \approx \frac{4\pi j'_{\nu'_{\text{syn}}}}{h\nu'_{\text{syn}}} \frac{\Delta R}{c}, \quad (32)$$

The function $F_{\text{KN}}(g, q)$ is a correction factor of the Klein-Nishina effect (Blumenthal & Gould 1970).

$$F_{\text{KN}}(g, q) = 2q \ln q + (1 + 2q)(1 - q) + \frac{8g^2 q^2}{1 + 4gq} (1 - q), \quad (33)$$

where we define

$$f \equiv \frac{h\nu'}{\gamma m_e c^2}, \quad (34)$$

$$q \equiv \frac{f}{4g(1-f)}. \quad (35)$$

Very high-energy gamma rays are usually absorbed through pair creation. The cross-section for $\gamma\gamma$ annihilation is given by (Gould & Schröder 1967)

$$\sigma_{\gamma\gamma} = \frac{3\sigma_{\text{T}}}{8s^2} \left[(2s + 2 - s^{-1}) \ln(\sqrt{s} + \sqrt{s-1}) - (s+1)(1-s^{-1}) \right], \quad (36)$$

where

$$s \equiv \frac{\epsilon_1 \epsilon_2}{2m_e^2 c^4}, \quad (37)$$

is the normalised energy interacting between two photons with energy ϵ_1 and ϵ_2 . Because we assume the target photon is distributed isotropic for simplicity, the expression of Eq. (36) has no information about the scattering angle. Then, the optical depth of the pair creation can be calculated as

$$\tau_{\gamma\gamma}(\epsilon_1) = \Delta R \int_{\epsilon(s>1)}^{\infty} d\epsilon_2 \sigma_{\gamma\gamma}(\epsilon_1, \epsilon_2) n_{\nu'_{\text{syn}}}(\epsilon_2). \quad (38)$$

The lower bound of the energy integration corresponds to the minimum interaction energy threshold. We neglect radiation from secondary particles for simplicity. Then, the isotropic-equivalent flux is written as

$$F_{\text{SSC},\nu}(t_{\text{obs}}) = (1+z) \int \frac{R^2 d\Omega}{d_L^2} \mathcal{D}^3 \Delta R \frac{j'_{\text{SSC},\nu'}}{\tau_{\gamma\gamma}} (1 - \exp(-\tau_{\gamma\gamma})). \quad (39)$$

3 FORWARD SHOCK EMISSION

In this section, we study effects of the magnetic acceleration on the dynamics and radiation from the forward shock. We simulate a single relativistic ejecta plunging into a homogeneous low-magnetized ambient medium. The interaction between the ejecta and the medium generates a strong forward shock propagating into the medium. The initial magnetic energy of the ejecta is converted into the kinetic and thermal energy of the shocked ambient medium. This energy transfer is due to the magnetic pressure expansion (Kusafuka et al. 2023).

Simulations with a very high Γ (such as $\Gamma = 100$) are very hard to carry out. First, we simulate the shocks with $\Gamma_0 = 10$. Then, based on the simulation results, We attempt to establish a semi-analytic formulation for a higher Γ in Section 5, and discuss observational appearances in Section 6.

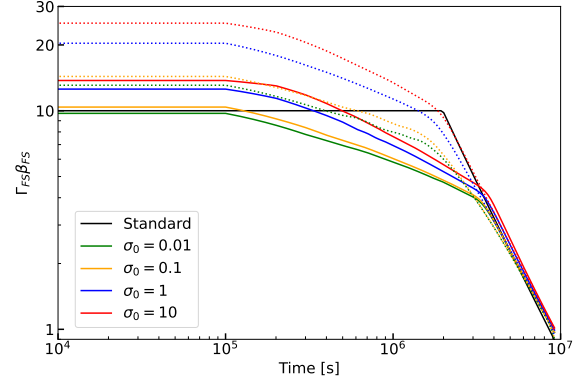


Figure 1. The time evolution of $\Gamma\beta$ of the shocked ambient medium just behind the forward shock. The parameters are $E_0 = 10^{50}$ erg, $\Gamma_0 = 10$, and $n_0 = 1 \text{ cm}^{-3}$. The solid line represents the thick shell case and the dotted one represents the thin shell case. Each coloured line corresponds to a different initial magnetization σ_0 . The black line shows the frequently used approximation (standard model) in the thin shell case. The break time scale of the standard model is the deceleration time t_{dec} defined by Eq. (9).

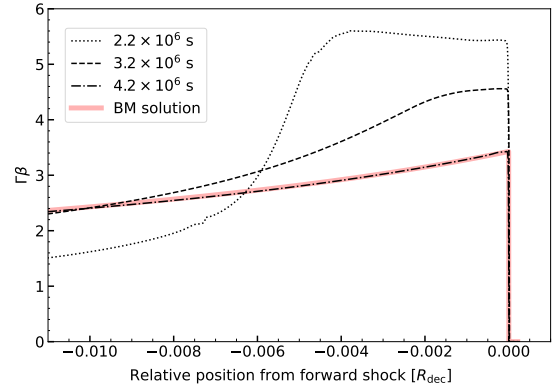


Figure 2. The radial profiles of $\Gamma\beta$ around the end of the transition phase for $\sigma_0 = 10$ showing the temporal evolution. The rarefaction wave from the rear edge of the ejecta approaches to the forward shock front, finally achieving the BM solution as the red mask expressed.

3.1 Dynamics of the forward shock

In the simplest approximation, until the deceleration time scale $t_{\text{dec}} \approx R_{\text{dec}}/c$, the dynamics of the forward shock is free expansion with constant speed. Beyond t_{dec} , the forward shock evolves adiabatically with decaying $\Gamma\beta$ given by the Blandford-McKee (BM) solution (Sari & Piran 1995; Zhang & Kobayashi 2005; Giannios et al. 2008). The BM solution is a self-similar solution for an ultra-relativistic outflow from a point-like explosion. According to this solution, the Lorentz factor of the shock front Γ_{FS} evolves as $\Gamma_{\text{FS}} \propto t^{-3/2} \propto t_{\text{obs}}^{-3/8}$ (Blandford & McKee 1976). For the thick shell case (Sari & Piran 1995), the propagation of the reverse shock affects the evolution of Γ_{FS} before the BM stage as $\Gamma_{\text{FS}} \propto t^{-1/2} \propto t_{\text{obs}}^{-1/4}$ (Sari 1997). Hereafter, we denote the above description of the Lorentz factor evolution as the "standard" model.

Our numerical results in Figure 1 show different time evolutions

of Γ_{FS} from the standard model, where Γ_{FS} is estimated at the radius where the gas pressure becomes maximum behind the shock front. The differences in the initial Lorentz factor are due to the impulsive acceleration (Granot et al. 2011): the magnetic pressure accelerates the head of the ejecta. The acceleration of the forward shock lasts until the reverse shock ignition. A detailed description of the transition from the acceleration phase to the coasting phase will be given in §5.2.

Unfortunately, the forward shocked region cannot be resolved in the early stage of the coasting phase. However, the reverse shock is resolved so that the Lorentz factor at the end of the coasting phase Γ_i is roughly consistent with the analytical estimate in §5.2. To calculate radiation from the forward shock in the coasting stage, we interpolate physical quantities such as the Lorentz factor. As the shocked region is resolved just after the end of the coasting phase, the Lorentz factor is interpolated as a constant Γ_i before this time following the definition of the coasting phase. The number density n_{FS} and internal energy density ϵ_{FS} in the coasting phase are obtained from the Rankine-Hugoniot relation (Blandford & McKee 1976) as

$$n_{\text{FS}} = (4\Gamma_i + 3)n_0, \quad (40)$$

$$\epsilon_{\text{FS}} = (4\Gamma_i + 3)(\Gamma_i - 1)n_0 m_p c^2. \quad (41)$$

Our results show two breaks for both the thin and thick shell cases. The first break at the end of the coasting phase appears an order of magnitude faster than the deceleration time (the break time for the standard model). The coasting phase ends when the density of the reverse shocked region decreases to $\sim \Gamma_i^2 n_0 / (1 + \sigma_{\text{RS}})$, where the subscript RS denotes the quantity in the reverse shocked region (see discussion in §5.2). This transition radius R_T is similar to the radius R_N defined in Sari & Piran (1995); the reverse shock becomes relativistic at $R = R_N$ in non-magnetized cases. In high- σ cases, the reverse shock is already relativistic, and the reverse shock crossing radius R_Δ can be smaller than R_T even in the thick shell case.

As discussed in Kusafuka et al. (2023), from $R = R_T$ to the second break at $R = R_{\text{BM}}$, the deceleration is gradual compared to the BM solution owing to the finite thickness of the ejecta. Figure 2 shows the profile of $\Gamma\beta$ just before the second break. At $t = 2.2 \times 10^6$ s, the reverse shock already crossed the ejecta. The rarefaction wave gradually catches up with the forward shock front. During this phase, the deceleration of the forward shock is suppressed by the pressure of the reverse shocked region. We call this phase the "transition phase" ($R_T < R < R_{\text{BM}}$), which is different from the reverse shock crossing phase between R_N and R_Δ . This $\Gamma\beta$ -evolution in the transition phase will modify light curves in GRB early afterglows.

The dynamics in the transition phase might be described by BM solution with internal energy injection (Zhang et al. 2006; Gao et al. 2013; van Eerten 2014) as

$$\Gamma_{\text{FS}} \propto t^{-\frac{1}{3+s}}, \quad (42)$$

where s denotes the index for the energy increase with the decelerating Γ , $E \propto \Gamma^{1-s}$. According to our results, the slope of the transition phase has a slight dependence on the initial magnetization as $\Gamma_{\text{FS}} \propto t^{-\alpha(\sigma_0)}$. The index $\alpha(\sigma_0) = 3/(1+s)$ ranges from 0.32 to 0.48 as σ_0 increases. This in turn means the injection rate s ranges from 5 to 8 as σ_0 decreases. This magnetization dependence results in the different rising slopes in the light curve of early afterglows. The energy injection rate can be estimated by the pressure balance at the contact discontinuity. We will derive the analytical expression of the transition phase in Section 5.

The transition phase lasts until the rarefaction wave from the rear edge of the ejecta reaches the forward shock front at $R = R_{\text{BM}}$

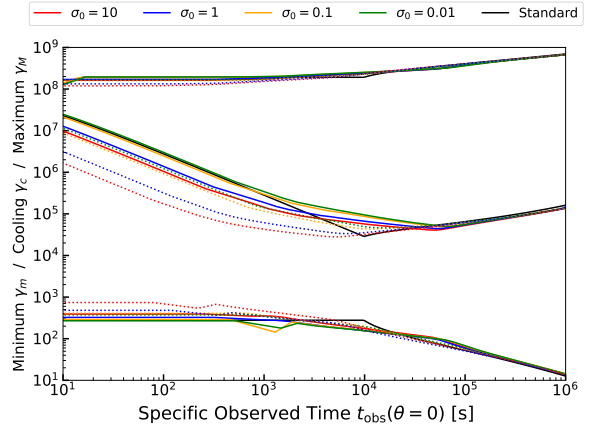


Figure 3. The time evolution of the characteristic Lorentz factors of accelerated electrons in the forward shock region. From the top, middle, and bottom, we show the maximum, cooling, and minimum Lorentz factor, respectively. The parameters are $E_0 = 10^{50}$ erg, $\Gamma_0 = 10$, $n_0 = 1 \text{ cm}^{-3}$, $\epsilon_e = 0.1$, and $\epsilon_B = 0.01$. The solid and dotted lines are for the thick and thin cases. Each coloured line corresponds to a different initial magnetization σ_0 . The black lines are for the standard model.

(Kobayashi & Sari 2000; Mimica et al. 2009; van Eerten 2014; Kusafuka et al. 2023). Figure 1 shows that the second break of $\Gamma\beta$ appears at $t \approx 4 \times 10^6$ s for the thick shell case and 2×10^6 s for the thin shell case. These break timescales are almost independent of the initial magnetization of the ejecta. Since the second break time scale strongly depends on the initial width of the ejecta, we may infer the radial structure of the ejecta. For $R > R_{\text{BM}}$, the radial profile of $\Gamma\beta$ agrees with the analytical Blandford-McKee solution (red line in Figure 2). The evolution of the physical quantities for $R > R_{\text{BM}}$ is the same as the standard model.

3.2 Spectrum evolution

Based on the Lorentz factor evolution of the forward shock, we can calculate the characteristic Lorentz factors of the non-thermal electrons from Eqs. (11), (12), and (21). The result is shown in Figure 3. In our cases, the electron spectra are always slow cooling ($\gamma_m < \gamma_c$). In the high- σ case, the high value of the initial Lorentz factor makes the minimum Lorentz factor larger and the cooling Lorentz factor smaller than the standard model. However, these differences gradually disappear in the late phase.

Then, we produce the corresponding observed radiation spectra as shown in Figure 4. The radiation spectra in the transition phase are shown in the left panel, while those in the BM phase are exhibited in the right panel. The three spectral breaks in the synchrotron component are characterised by three frequencies: minimum $\nu_m \equiv \nu(\gamma_m)$, cooling $\nu_c \equiv \nu(\gamma_c)$, and maximum frequency $\nu_M \equiv \nu(\gamma_M)$. The spectral slope is roughly followed by the analytical result of Sari et al. (1998)

$$\nu F_\nu \propto \begin{cases} \nu^{4/3} & \nu < \nu_m \\ \nu^{-\frac{p-3}{2}} & \nu_m < \nu < \nu_c \\ \nu^{-\frac{p-2}{2}} & \nu_c < \nu < \nu_M \end{cases}. \quad (43)$$

The Klein-Nishina effect makes the SSC component softer than the synchrotron component in the highest energy. Since the optical photon number density is not so high, the $\gamma\gamma$ annihilation process

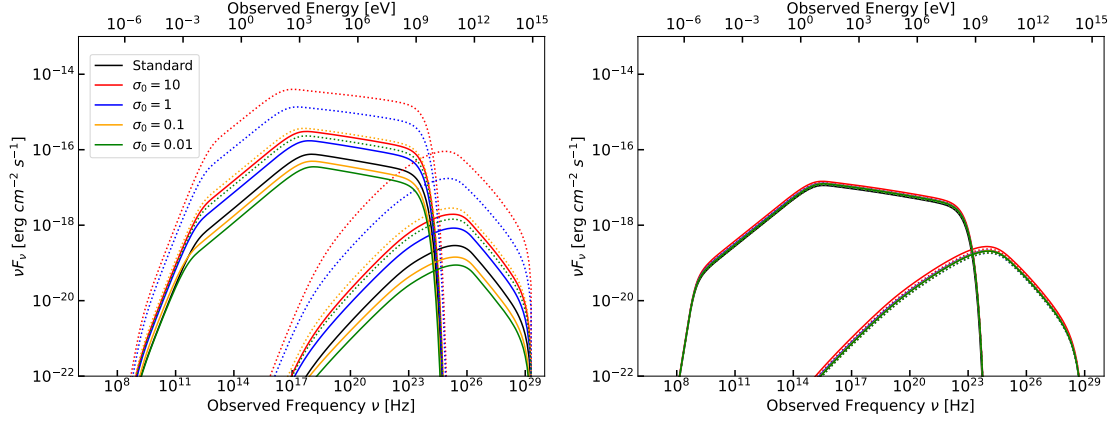


Figure 4. The observed spectrum of the forward shock radiation at $t_{\text{obs}} = 2.0 \times 10^3$ s. The parameters are $E_0 = 10^{50}$ erg, $\Gamma_0 = 10$, $n_0 = 1 \text{ cm}^{-3}$, $\epsilon_e = 0.1$, $\epsilon_B = 0.01$, and $z = 1.0$. The low-frequency component is the synchrotron radiation and the high-frequency component is the SSC radiation. The solid lines represent the thick shell cases and the dotted ones represent the thin shell cases. Each coloured line corresponds to a different initial magnetization σ_0 . The black line shows the standard model. The right panel: the same figure at $t_{\text{obs}} = 1.0 \times 10^6$ s.

does not affect the spectrum in our cases. The SSC cutoff energy reflects the maximum accelerated energy of electrons.

The higher Lorentz factor for the high- σ models make the early phase radiation an order of magnitude brighter than the standard model as shown in the left panel of Figure 4. In the BM phase, no difference appears among the models as shown in the right panel of Figure 4.

3.3 Multi-wavelength light curve

Figure 5 shows the light curves for the forward shock radiation. As the late-phase forward shock dynamics are independent of initial magnetization and width, and only depend on the initial energy, the late-phase light curves of all models are consistent with the standard model. The onset time scale for frequencies higher than ν_m corresponds to the beginning of the BM phase depending on the initial width and magnetization of the ejecta. While the onset time scale has been used to estimate the initial bulk Lorentz factor, as our results suggest, the standard model overestimates the Lorentz factor if the initial width is thick. For $\nu_{\text{obs}} < \nu_m$, the flux increases as far as the time when $\nu = \nu_m$.

The major difference between our calculations and the standard model is the existence of the transition phase, which is significantly longer than the reverse shock crossing time. The flux rises gradually compared to that of the coasting phase. The observed flux at the transition phase evolves as $\nu F_\nu \propto t_{\text{obs}}^{\beta(\sigma_0)}$, where $\beta(\sigma_0) = 0.5 \sim 2.0$ depending on the initial magnetization. Because this phase lasts until the rarefaction wave catches up timescale, the duration of the transition phase strongly depends on the initial width of the ejecta. These dependencies of the initial width and magnetization are helpful for the investigation of the initial physical conditions of the ejecta. In the coasting phase, the peak flux follows

$$\nu F_\nu \propto \begin{cases} t_{\text{obs}}^2 & \nu < \nu_a \\ t_{\text{obs}}^3 & \nu_a < \nu < \nu_c \\ t_{\text{obs}}^{\frac{10-3p}{4-p}} & \nu_c < \nu < \nu_M \end{cases} \quad (44)$$

for synchrotron radiation (ν_a is SSA frequency), and

$$\nu F_\nu \propto \begin{cases} t_{\text{obs}}^4 & \nu < \nu_c^{\text{IC}} \\ t_{\text{obs}}^{\frac{12-4p}{4-p}} & \nu_c^{\text{IC}} < \nu < \nu_M^{\text{IC}} \end{cases} \quad (45)$$

for the SSC emission. (Sari & Piran 1999b; Sari & Esin 2001; Wu et al. 2005). For the thin shell case of $\sigma_0 = 10$, the magnetic acceleration boosts the Lorentz factor of the forward shock by factor 3 according to Figure 1. From Eq. (24), the observed time becomes shorter by a factor of $\Gamma^2 \sim 10$. If we compare the observed flux at the same observed time, the synchrotron flux of the thin shell case of $\sigma_0 = 10$ is brighter than the standard model prediction by $\sim 10^{3-4}$, which is due to the high Γ and Doppler boost effects. The SSC flux is also enhanced by $\sim 10^{3.5-5.5}$ than that of the standard model. Such bright early afterglows can be the best target for future follow-up observations.

4 REVERSE SHOCK EMISSION

In this section, we study effects of the magnetic acceleration on the dynamics and radiation of the reverse shock. The interaction between the ejecta and the medium generates a reverse shock propagating backwards in the ejecta. The initial kinetic energy of the ejecta is converted into the magnetic and thermal energy of the shocked ejecta. The reverse shock crossing time becomes shorter as the magnetization increases (Zhang & Kobayashi 2005; Mimica et al. 2009; Kusafuka et al. 2023).

4.1 Dynamics of the reverse shock

We define the time at which the reverse shock crosses the ejecta as t_Δ . In a hydrodynamic case ($\sigma_0 = 0$), Sari & Piran (1995) provided an analytical formula of t_Δ as

$$t_\Delta(\sigma_0 = 0) = \Gamma_0^{1/2} R_{\text{dec}}^{3/4} \Delta_0^{1/4}, \quad (46)$$

where Δ_0 is the shell thickness in the ambient medium rest frame. Since a magneto-sonic speed becomes faster in a magnetized medium, the reverse shock crossing time $t_\Delta(\sigma_0)$ becomes shorter

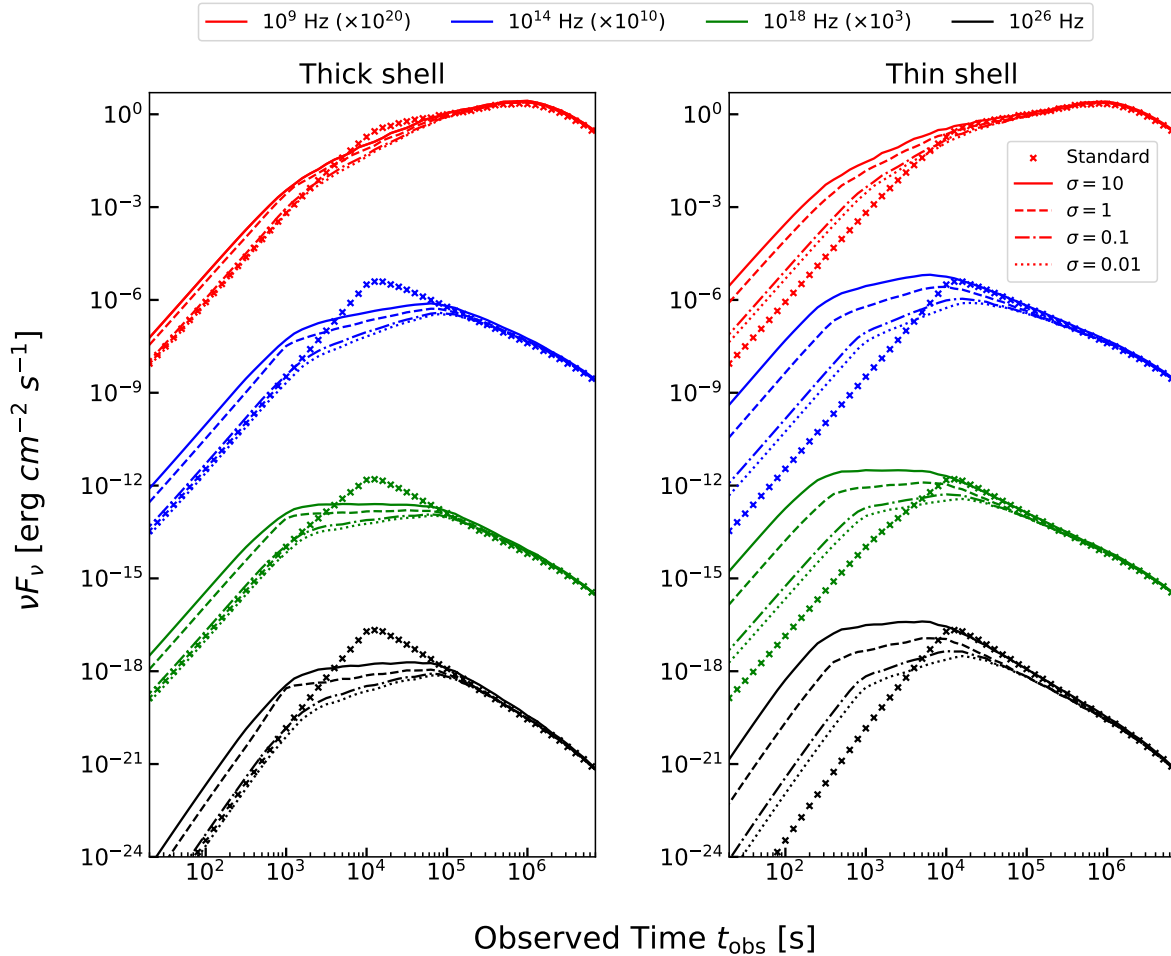


Figure 5. The light curves for the case of the forward shock radiation. The left panel shows the thick shell cases while the right panel shows the thin shell cases. The solid, dashed, dash-dotted, dotted lines correspond to the case of $\sigma_0 = 10, 1, 0.1, 0.01$, respectively. The lines denoted with crosses represent the standard model. Each coloured line corresponds to a different observed frequency; red: radio (10^9 Hz), blue: optical (10^{14} Hz), green: X-ray (10^{18} Hz), black: high-energy γ -ray (10^{26} Hz). All plots except for the high-energy γ -ray have arbitrary offsets for convenience.

(Zhang & Kobayashi 2005; Giannios et al. 2008) as

$$t_{\Delta}(\sigma_0) \approx t_{\Delta}(\sigma_0 = 0)(1 + \sigma_0)^{-1/2}. \quad (47)$$

As shown in Figure 6, the above formula well agrees within $\sim 10\%$ with numerical simulations (e.g. Mimica et al. 2009; Kusafuka et al. 2023). In GRB afterglows, the reverse shock crossing time $t_{\Delta}(\sigma_0)$ determines the time of the peak flux of the reverse shock radiation (Zhang & Kobayashi 2005). Our results confirm that high- σ ejecta leads to the early peak time of the reverse shock radiation.

Figure 7 shows the time evolution of $\Gamma\beta$ of the reverse shock, which is estimated at the radius where the Lorentz factor becomes maximum behind the shock front. The data is plotted from a reverse shock ignition time to the crossing time. The reverse shock dynamics are almost synchronised with the forward shock dynamics. In high- σ cases, the magnetic acceleration boosts the Lorentz factor of the reverse shock. Until the transition phase, the reverse shock speed is almost constant. Then, it decelerates gradually as $t^{-\beta(\sigma_0)}$. The index $\beta(\sigma_0)$ ranges from 0.33 to 0.5 as σ_0 increases, which is almost the same value for the case of the forward shock. From our simulation, we confirm the relation $\Gamma_{\text{RS}} \approx \Gamma_{\text{FS}}$ (Sari & Piran 1995; Zhang & Kobayashi 2005).

Relative Lorentz factor of the reverse shock Γ_{rel} is calculated by

(Sari & Piran 1995; Zhang & Kobayashi 2005)

$$\Gamma_{\text{rel}} = \Gamma_{\text{RS}}\Gamma_{\text{ejecta}}(1 - \beta_{\text{RS}}\beta_{\text{ejecta}}) \approx \frac{1}{2} \left(\frac{\Gamma_{\text{ejecta}}}{\Gamma_{\text{RS}}} + \frac{\Gamma_{\text{RS}}}{\Gamma_{\text{ejecta}}} \right). \quad (48)$$

In the simulation data, the Lorentz factor of the unshocked ejecta Γ_{ejecta} is estimated at the radius where the Lorentz factor becomes maximum. Because the speeds are almost the same order $\Gamma_{\text{RS}} \sim \Gamma_{\text{ejecta}}$ in our simulation results, the strength of the reverse shock is weak $\Gamma_{\text{rel}} \sim 1$ compared to the forward shock $\Gamma_{\text{FS}} \gg 1$. As is well known, the higher magnetization ($\sigma \geq 1$), implying a magneto-sonic speed is $\approx c$, leads to a weak shock, i.e. a less energy dissipation of the shocked region (Kennel & Coroniti 1984). Thus, the reverse shock radiation is suppressed for $\sigma \gg 1$ (Zhang & Kobayashi 2005).

4.2 Multi-wavelength radiation

Based on the Lorentz factor evolution of the reverse shock, we can calculate the characteristic Lorentz factor of non-thermal electrons from Eqs. (11), (12), and (21). The result is shown in Figure 8. In our simulations, the electron spectra are always slow cooling ($\gamma_m < \gamma_c$) due to the numerically limited parameter range (especially the initial

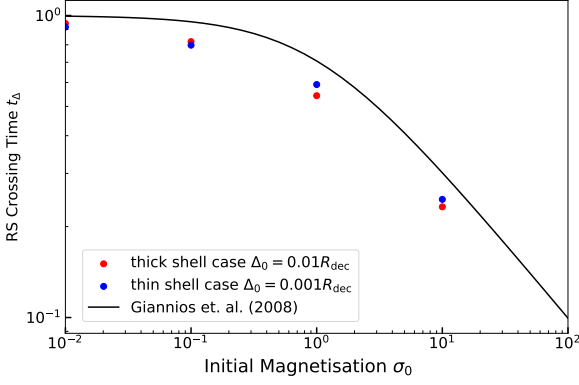


Figure 6. The reverse shock crossing timescale as a function of the initial magnetization. The solid line is the analytical estimate given by Eq. (47).

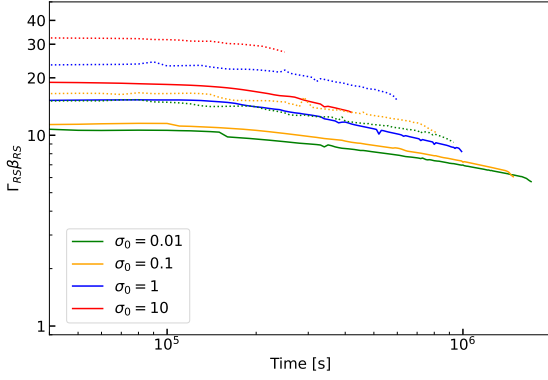


Figure 7. The time evolution of $\Gamma\beta$ of the shocked ejecta just behind the reverse shock until the reverse shock crossing time t_Δ . The solid line represents the thick shell case and the dotted one represents the thin shell case. Each coloured line corresponds to a different initial magnetization σ_0 .

energy). Since the relative Lorentz factor of the reverse shock is very weak, the minimum Lorentz factor of electrons γ_m is almost 1 in the coasting phase, then gradually increases in the transition phase for low magnetization cases. The cooling Lorentz factor evolves in different ways depending on the initial magnetization. For high magnetization cases, the initial plateau evolution of γ_c is due to the weakness of the reverse shock compression of the magnetic field. Then, it gradually decreases as ejecta decelerates. For low magnetization cases, on the other hand, relatively strong reverse shock can compress the ejecta magnetic field resulting in the decreasing feature of γ_c .

The corresponding observed radiation spectra at 2.5×10^3 s are shown in Figure 9. Due to the relatively high magnetization level compared to the forward shock case, the SSC peak flux is a few orders of magnitude lower than the synchrotron peak flux. The synchrotron spectral shape is roughly followed by Eq. (43), but hard spectra $\nu F_\nu \propto \nu^{3.5}$ due to SSA is seen in the low-energy region. Because ν_m is an order of magnitude smaller than that of the forward shock, the reverse shock emission can emerge in the low-frequency region for low-magnetized cases.

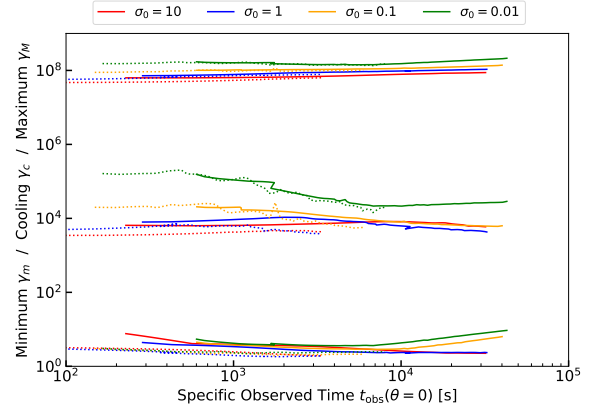


Figure 8. The time evolution of the characteristic Lorentz factors of accelerated electrons in the reverse shock region. From the top, middle, and bottom, we show the maximum, cooling, and minimum Lorentz factor, respectively. The parameters are $E_0 = 10^{50}$ erg, $\Gamma_0 = 10$, $n_0 = 1 \text{ cm}^{-3}$, $\epsilon_e = 0.1$, and $\epsilon_B = 0.01$. The solid and dotted lines are for the thick and thin shell cases. Each coloured line corresponds to a different initial magnetization σ_0 .

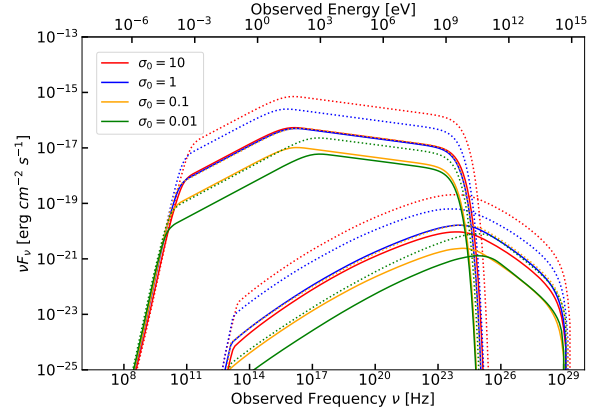


Figure 9. The observed spectrum of the reverse shock radiation at $t_{\text{obs}} = 2.5 \times 10^3$ s. The low-frequency component is the synchrotron radiation and the high-frequency component is the SSC radiation. The solid lines represent the thick shell cases and the dotted ones represent the thin shell cases. Each coloured line corresponds to a different initial magnetization σ_0 . The black line shows the standard model.

Figure 10 shows the light curves for the reverse shock radiation. All models achieve the peak flux at the reverse shock crossing time. Even after the reverse shock crossing time, the high latitude emission lasts for a while, making decreasing features. Due to the magnetic acceleration, the peak flux of the thin shell cases is slightly higher than that for the thick shell cases. The rising slope has a slight dependence on the initial magnetization σ_0 , which might be constrained by early follow-up observations. For higher magnetization cases, the weak energy dissipation at the reverse shock suppresses the emission flux. Besides the high latitude emission ceases faster for higher magnetization cases due to the short angular timescale $\sim R_{\text{RS}}/(c\Gamma_{\text{RS}}^2)$.

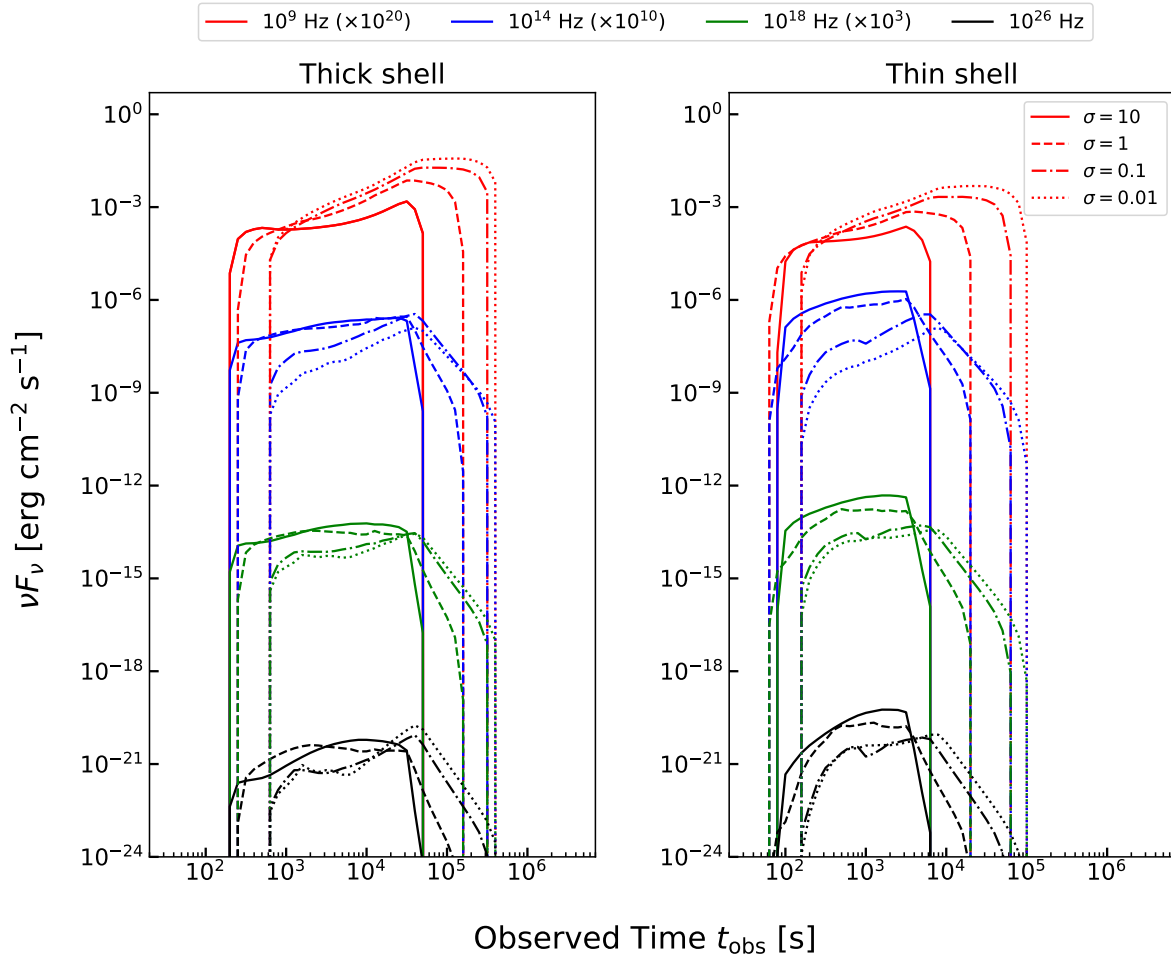


Figure 10. The light curves for the case of the reverse shock radiation. The left panel shows the thick shell cases while the right panel shows the thin shell cases. The solid, dashed, dash-dotted, dotted lines correspond to the case of $\sigma_0 = 10, 1, 0.1, 0.01$, respectively. Each coloured line corresponds to a different observed frequency; red: radio (10^9 Hz), blue: optical (10^{14} Hz), green: X-ray (10^{18} Hz), black: high-energy γ -ray (10^{26} Hz). All plots except for the high-energy γ -ray have arbitrary offsets for convenience.

5 SEMI-ANALYTICAL DESCRIPTION

Based on our simulation results, we provide an analytical description of the evolutions of the shocks and emissions. The following formulae include the effect of the initial magnetic acceleration and the transition phase as a function of the initial magnetization and width of the ejecta. Figure 11 is a schematic picture of the forward shock dynamics. We explain the details and feasibility of our formulae below.

5.1 Reverse shock ignition time

In high- σ cases, the impulsive acceleration of the ejecta is expected (Lyutikov 2010; Granot et al. 2011; Komissarov 2012). Initially, the magnetic pressure in the ejecta is higher than that of the shocked ambient medium. When the gas pressure of the shocked ambient medium overwhelms the total pressure of the ejecta, a reverse shock can ignite (Granot 2012a,b). Since the reverse shock decelerates the ejecta, the acceleration of the forward shock is terminated at the reverse shock ignition time t_{RS} . The pressure balance at the contact

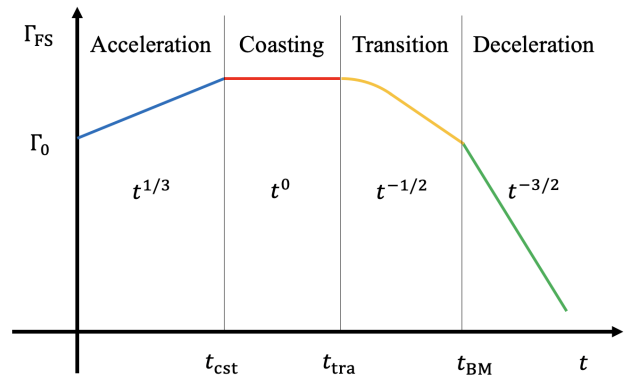


Figure 11. A schematic description of the evolution of the forward shock Lorentz factor. Our model consists of 4 phases: acceleration, coasting, transition, and deceleration. The timescale t_{cst} , t_{tra} , and t_{BM} are switching timescales between each phase (see the text in detail).

discontinuity (e.g. Zhang & Kobayashi 2005) is written as

$$\frac{B'_{ej}{}^2}{8\pi} = \frac{4}{3}\Gamma_{FS}^2 n_0 m_p c^2, \quad (49)$$

where B_{ej} is the magnetic field of the ejecta. This equation can be written through magnetization as

$$\sigma_{ej} = \frac{8}{3} \frac{\Gamma_{FS}^2 n_0}{n_{ej}}, \quad (50)$$

where σ_{ej} and n_{ej} are the magnetization and number density of the ejecta, respectively. From number conservation, we can estimate the number density of the ejecta as

$$n_{ej,0}(t) = \frac{E_0}{4\pi\Delta_0(1+\sigma_0)\Gamma_0^2 m_p c^2} (R_0 + ct_{RS})^{-2}. \quad (51)$$

For low magnetization cases ($\sigma_0 \leq 1$), we assume $\sigma_{ej} \approx \sigma_0$. Even for high magnetization cases ($\sigma_0 \geq 1$), a rarefaction wave reduces the magnetic pressure of the ejecta, resulting in an ignition of a reverse shock. In the impulsive acceleration, the time evolution of the typical Lorentz factor and the magnetization of the ejecta are (Lyutikov 2010; Granot et al. 2011)

$$\Gamma_{ej}(t) = \Gamma_0 (1 + ct\sigma_0/\Delta_0)^{1/3}, \quad (52)$$

and

$$\sigma_{ej}(t) = \sigma_0 (1 + ct\sigma_0/\Delta_0)^{-1/3}, \quad (53)$$

respectively. Besides, the number density of the ejecta decreases as

$$n_{ej}(t) = n_{ej,0} (1 + ct\sigma_0/\Delta_0)^{-1/3}. \quad (54)$$

While the energy-weighted Lorentz factor evolves as discussed above (see also, Komissarov 2012; Kusafuka et al. 2023), Lyutikov (2010) and Granot (2012b) claim that the maximum Γ of the forward shock is accelerated to $\sim \Gamma_0\sigma_0$ instantaneously for the step-function profile of σ expanding into vacuum. For predicting the emission property in the actual GRB jets, the approximate method has not been established. In this paper we adopt the energy-weighted behavior as above. To make a semi-analytic model based on our simulation results, we adopt $\Gamma_{FS} \approx \Gamma_{ej}$, and then obtain the following fifth-order equation from Eq. (49),

$$(ct_{RS} + R_0)^3 (ct_{RS} + \Delta_0/\sigma_0)^2 = C, \quad (55)$$

where

$$C = \sqrt{\frac{\Delta_0}{\sigma_0} \left(\frac{R_{dec}^3}{8\Gamma_0^2(1+\sigma_0)} \right)^3}. \quad (56)$$

If a condition $R_0^3(\Delta_0/\sigma_0)^2 \leq C$ is satisfied, there exists only one physical solution for t_{RS} in $0 < t_{RS} < C^{1/5}$, otherwise we should take $t_{RS} = 0$. Adopting the obtained t_{RS} into Eq. (52), the saturated Lorentz factor of the ejecta Γ_{sat} is estimated as

$$\Gamma_{sat} = \min(\Gamma_{ej}(t = t_{RS}), \Gamma_0(1 + \sigma_0)). \quad (57)$$

5.2 Shock waves evolutions in the transition phase

In the coasting phase, $\Gamma_{FS} = \Gamma_{RS} = \Gamma_{sat}$. As the ejecta expands, the pressure in the reverse shocked region decreases, but balances with the gas pressure of the shocked ambient medium as (Zhang & Kobayashi 2005)

$$(1 + \sigma_{RS})(4\Gamma_{rel} + 3)(\Gamma_{rel} - 1)n_{ej,1} = (4\Gamma_{FS} + 3)(\Gamma_{FS} - 1)n_0. \quad (58)$$

Combining these conditions with Eq. (48), we obtain the evolution in the transition phase as

$$\Gamma_{FS}(t) = \Gamma_{RS}(t) \approx \frac{\Gamma_{sat}}{\left[1 + 2\Gamma_{sat} \sqrt{\frac{n_0}{n_{ej,1}(1+\sigma_{RS})}} \right]^{1/2}}, \quad (59)$$

where $n_{ej,1}$ is the number density of the unshocked ejecta after the end of the impulsive acceleration and σ_{RS} is the magnetization of the shocked ejecta. In the limit of the non-magnetized case ($\sigma_0 = 0$), the expression agrees with the same equation given in Panaitescu & Kumar (2004); Murase (2007); Shen & Matzner (2012).

In the coasting phase, the second term of the denominator in Eq. (59) is negligible. That term becomes unity at the onset of the transition phase, $t = t_{tra}$. According to our results, the magnetization of the shocked ejecta is roughly the same as the initial magnetization, so we set $\sigma_{RS} \approx \sigma_0$. The number density of the unshocked ejecta is roughly estimated from combining Eq. (51), (54), (57) as

$$n_{ej,1}(t) = \frac{E_0}{4\pi\Delta_0(1+\sigma_0)\Gamma_{sat}\Gamma_0 m_p c^2} (R_0 + ct)^{-2}. \quad (60)$$

Then, we have the following second-order equation by equating the first and the last terms in the denominator of Eq. (59)

$$(ct_{tra} + R_0)^2 \approx \frac{R_{dec}^3 \Gamma_0}{12\Delta_0 \Gamma_{sat}^3}. \quad (61)$$

However, the onset time of the transition phase t_{tra} does not well characterise the shock evolution. In the coasting and transition phases, the Lorentz factor evolves following Eq. (59), which produces a gradual evolution with Eq. (60) rather than the sharp break at $t = t_{tra}$.

Since the factor $n_{ej,1}(1 + \sigma_{RS})$ decreases as $\propto t^{-2}$, the asymptotic behaviour of Eq. (59) in the transition phase becomes

$$\Gamma_{FS} \propto t^{-1/2}. \quad (62)$$

This index is roughly consistent with our numerical results. The shocked ejecta sustains the forward shocked region. Since the energy injection from the shocked ejecta to the forward shock mitigates the forward shock deceleration (van Eerten 2014), the transition phase lasts even after the reverse shock crossing.

In the acceleration phase, the Lorentz factor Γ_{FS} is the same as that of the ejecta Γ_{ej} expressed by Eq. (52). Then, Γ_{FS} gradually deviates from Γ_{ej} and transits to the behaviour expressed by Eq. (59). Therefore, the maximum value of Γ_{FS} is smaller than Γ_{sat} given by Eq. (57). To obtain the maximum of Γ_{FS} , we first define the beginning time of coasting phase t_{cst} by the cross point of the two curves expressed by Eq. (52) and Eq. (59) as

$$\Gamma_{ej}(t = t_{cst}) = \Gamma_{FS}(t = t_{cst}). \quad (63)$$

As $\Gamma_{FS} < \Gamma_{sat}$, the time t_{cst} is earlier than t_{RS} . Adopting the obtained t_{cst} to Eq. (52), the maximum value of Γ_{FS} is given by

$$\Gamma_{max} = \Gamma_0(1 + ct_{cst}\sigma_0/\Delta_0)^{1/3}. \quad (64)$$

5.3 Transition to BM phase

The conventional deceleration radius is given by Eq. (9), which is independent of the initial width of the ejecta. However, our simulations suggest that the transition time to the BM phase t_{BM} is approximately determined by the time at which the rarefaction wave catches up with the forward shock front, which can be roughly obtained from

$$\Delta = \int_{t_\Delta}^{t_{BM}} (c - v_{FS,front}) dt \approx \int_{t_\Delta}^{t_{BM}} \frac{cdt}{4\Gamma_{FS}^2(t)}, \quad (65)$$

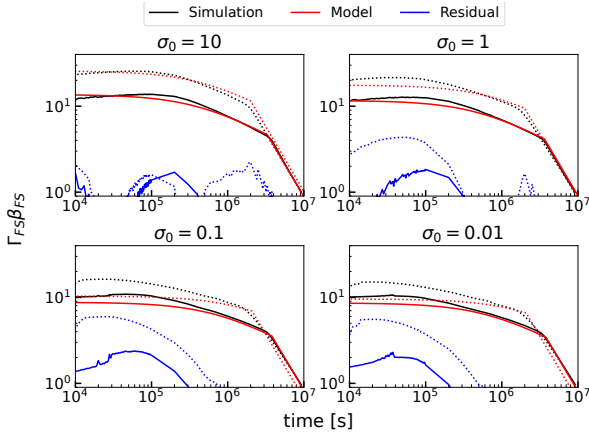


Figure 12. The evolutions of the forward shock Lorentz factors obtained by our semi-analytic estimate (red), numerical simulations (black), and their absolute residuals (blue). Each panel shows the dynamics with a different initial magnetization. The solid line corresponds to the thick shell case, while the dotted line corresponds to the thin shell case.

where $v_{\text{FS,front}} = c\sqrt{1 - 1/(2\Gamma_{\text{FS}}^2)}$ is the velocity of the forward shock front, and Δ is the total width of the shocked ejecta and shocked ambient medium at $t = t_{\Delta}$ given by Eq. (47). The time evolution of $\Gamma_{\text{FS}}(t)$ is given by Eq. (59). Since the rarefaction wave starts just after the reverse shock crossing time, we can estimate the total width as

$$\Delta = \Delta_0 + \int_0^{t_{\Delta}} (v_{\text{FS,front}} - v_{\text{FS}}) dt \simeq \Delta_0 + \int_0^{t_{\Delta}} \frac{cdt}{4\Gamma_{\text{FS}}^2(t)}, \quad (66)$$

where v_{FS} is the velocity just behind the forward shock. The evolution of Γ_{FS} is given by Eq. (52) and Eq. (59) for $t < t_{\text{cst}}$ and $t \geq t_{\text{cst}}$, respectively. If $\Gamma_{\text{FS}}(t_{\Delta})$ is larger than Γ_0 through magnetic acceleration or Δ_0 is sufficiently long, the onset time scale can be longer than the conventional deceleration time R_{dec}/c . This elongated transition phase is demonstrated by our simulated light curves as shown in Fig. 5.

5.4 Comparison with our simulation and model

Following the above procedures, we reproduce the dynamics of the forward shock using the same initial parameters in our numerical simulations. The results are shown in Figure 12. Although some slight differences appear in the early phase of the expansion, our semi-analytic model is almost consistent with our numerical simulation results. The differences are partially due to the finite temperature and finite resolution in our simulations. The thermal pressure expansion slightly accelerates the ejecta even for low magnetized cases. The forward shock is resolved with a few cells, which makes the Lorentz factor small compared to our model. In the late phase dynamics is well described by our model, which means that the afterglow peak time is indeed determined by the rarefaction wave catch-up time.

6 APPLICATION TO GRB EARLY AFTERGLOWS

Some GRB early afterglows have mysterious features - optical plateau, optical shallow rising, X-ray shallow decay, gamma-ray very steep rising, and so on (Fan & Piran 2006; Oates et al. 2009; van Eerten 2014; Zhang 2018; LHAASO Collaboration et al. 2023).

Some of those features may be due to the non-monotonic evolution of the bulk Lorentz factor as shown in the previous sections.

In this section, we discuss the observational implications for thick ($\Delta_0 = 4R_{\text{dec}}/\Gamma_0^2$) and thin shell ($\Delta_0 = R_0/\Gamma_0^2$) cases, with $\sigma_0 = 10^{-2}$ and $\sigma_0 = 10$. We fix the initial ejecta energy $E_0 = 10^{52}$ erg, initial Lorentz factor $\Gamma_0 = 100$, initial radius $R_0 = R_{\text{dec}}/\Gamma_0$, and ambient number density $n_0 = 1 \text{ cm}^{-3}$ with $\epsilon_e = 0.1$ for both the forward and reverse shocks. The value of ϵ_e in the forward shock is generally different from that of the reverse shock (e.g. Zhang & Kobayashi 2005; Ryan et al. 2020), but we choose the same value for simplicity. For the reverse shock, we estimate the turbulent magnetic field from the magnetization and the number density of the reverse shock. Meanwhile, $\epsilon_B = 0.01$ is adopted for the forward shock. In these parameter sets, the shell width gives the timescale $\Delta_0/c = 7.2 \times 10^2$ s for thick shell cases and $\Delta_0/c = 1.8$ s for thin shell cases. The other characteristic timescales are summarised in Table 1. For the low-magnetized thin shell case, the transition time is longer than the deceleration time $t_{\text{tra}} > t_{\text{BM}}$. No transition and acceleration phases appear in this case, hence the Lorentz factor evolution in this case is the same as the standard model. Even for $\Gamma_{\text{FS}} > 100$, given the evolution of the Lorentz factor calculated with the method in Section 5, we can produce model light curves of forward and reverse shock radiation following the same procedure written in Section 2.2. The results are shown in Figure 13. Due to the large Lorentz factor, the acceleration phase cannot be seen in $t_{\text{obs}} > 1$ s.

From our calculated light curves, we can estimate the coefficient κ connecting between t and t_{obs} :

$$t_{\text{obs}} = (1+z) \frac{t}{\kappa \Gamma_{\text{FS}}^2}. \quad (67)$$

At $t = t_{\text{BM}}$, we can find $\kappa = 4$ is the best fitting value for all the cases. As we have mentioned, a light curve break at $t = t_{\text{tra}}$ is hard to identify. At $t = t_{\text{cst}}$, we find $\kappa = 1$ for $\sigma_0 = 10$ cases (no acceleration phase for $\sigma_0 = 10^{-2}$). While $\kappa = 4$ is frequently used (Sari 1997; Sari et al. 1998, 1999) to produce light curve analytically, the coefficient κ is not always universal (e.g. Derishev & Piran 2021; Asano 2024).

6.1 Reverse shock radiation

Candidates of reverse shock components have been observed in radio to optical band from early afterglows, including the famous examples such as GRB 990123 (Sari & Piran 1999a), GRB 021004 (Kobayashi & Zhang 2003), GRB 080319B (Fraija & Veres 2018), GRB 130427A (Laskar et al. 2013), and GRB 190829A (Dichiara et al. 2022).

The reverse shock radiation plotted as the dotted line in Figure 13 is calculated from t_{RS} to t_{Δ} . We calculate the width of the reverse shocked region in the shocked region rest frame as

$$\Delta R(t) = \Gamma_{\text{RS}}(t) \int_0^t (\beta_{\text{ej}} - \beta_{\text{RS}}) c dt, \quad (68)$$

where β_{RS} is the velocity just behind the reverse shock in the engine-rest frame. The number and internal energy density of the reverse shocked region are calculated from Eqs. (48), and (60) as

$$n_{\text{RS}} = (4\Gamma_{\text{rel}} + 3)n_{\text{ej},1}, \quad (69)$$

$$\epsilon_{\text{RS}} = (\Gamma_{\text{rel}} - 1)n_{\text{RS}}, \quad (70)$$

respectively. Since the initial magnetization is large and the $\Gamma_{\text{rel}} \sim 1$, the magnetic field can be roughly estimated as

$$B'_{\text{RS}} = \sqrt{4\pi n_{\text{RS}} m_p c^2 \sigma_0}. \quad (71)$$

Table 1. Characteristic timescales and the maximum Lorentz factor in Section 6.

Model	t_{cst} [s]	t_{RS} [s]	t_{tra} [s]	t_{Δ} [s]	t_{BM} [s]	Γ_{max}
thick ($\sigma_0 = 10$)	2.0×10^3	3.7×10^3	1.7×10^4	7.7×10^5	6.3×10^6	306
thick ($\sigma_0 = 10^{-2}$)	-	1.1×10^4	2.4×10^5	2.5×10^6	5.4×10^6	100
thin ($\sigma_0 = 10$)	2.2×10^2	1.0×10^3	1.2×10^5	1.7×10^5	1.6×10^6	1040
thin ($\sigma_0 = 10^{-2}$)	-	1.5×10^4	5.1×10^6	5.7×10^5	1.2×10^6	100

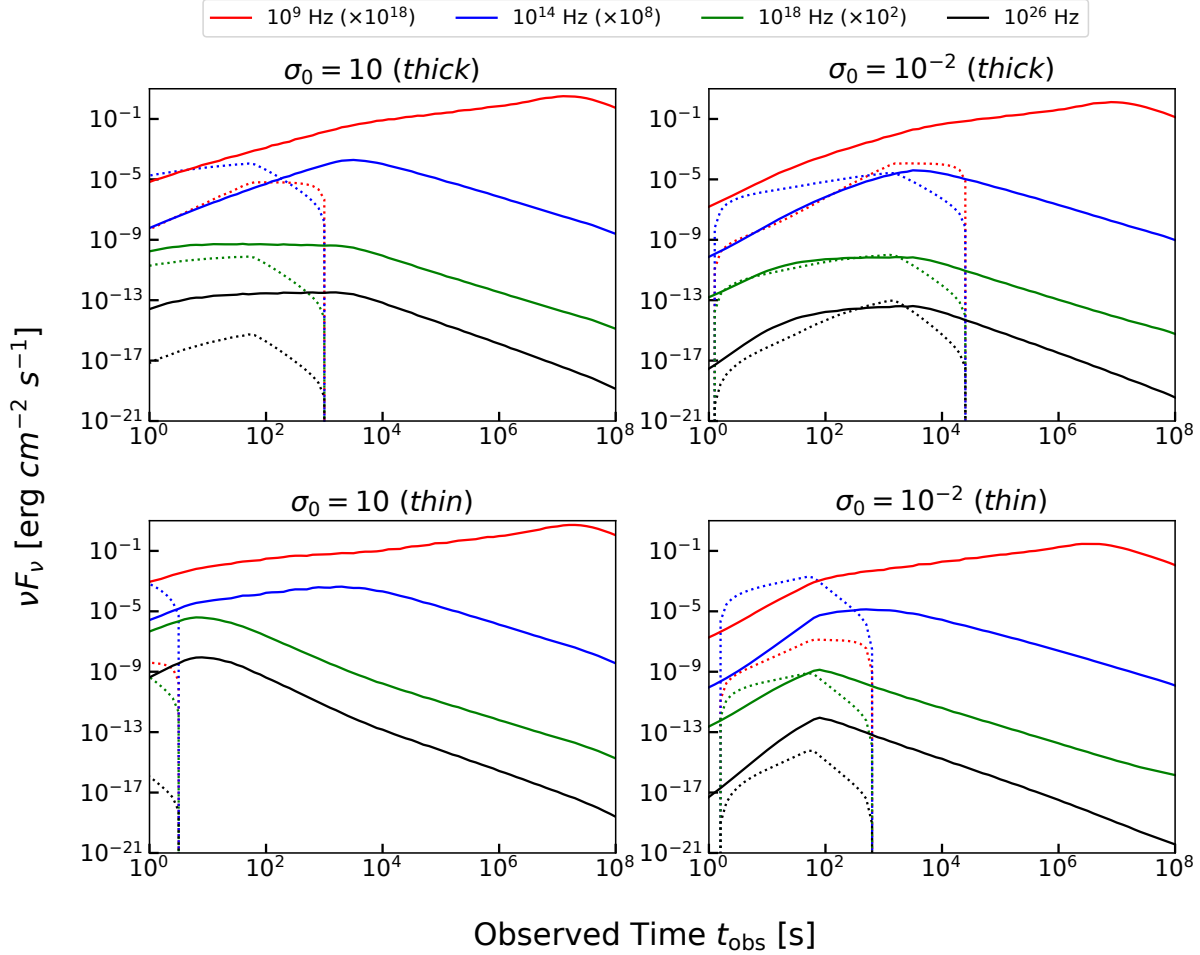


Figure 13. The observed light curve combined with the forward and reverse shock radiation. Each panel corresponds to the different initial magnetization and width of the ejecta. The rest of the parameters are the same for all models: $E_0 = 10^{52}$ erg, $\Gamma_0 = 100$, and $n_0 = 1 \text{ cm}^{-3}$. The solid line is the forward shock lightcurve and the dotted one is the reverse shock lightcurve. Each coloured line corresponds to a different observed frequency; red: radio (10^9 Hz), blue: optical (10^{14} Hz), green: X-ray (10^{18} Hz), black: γ -ray (10^{26} Hz). All data points except for the high-energy γ -ray have arbitrary offsets for convenience.

If the initial magnetization is significantly small as $\sigma_0 \ll 1$, we should estimate B'_{RS} from Eq. (13) with ϵ_B . In the reverse shock light curves, the peak time corresponds to t_{Δ} . Even after the peak, the high latitude emission lasts, producing decreasing features. For a thicker shell with a lower magnetization, the reverse shock ignition time determined by t_{RS} becomes earlier, and the end of the reverse shock emission becomes longer.

For high magnetization cases, the shock energy dissipation is inefficient producing the weak emission, and vice-versa. As shown in

the figures, the reverse and forward shock components can be comparable in optical, X-ray, and gamma-ray bands. The identification of the reverse shock emission in the lightcurve data is key to determining the magnetization. A caveat is that we assume efficient particle acceleration even in the high magnetization cases, though the diffusive shock acceleration may be inefficient for $\sigma > 10^{-3}$ (Sironi & Spitkovsky 2011; Sironi et al. 2013; Plotnikov et al. 2018). However, the magnetic reconnection may have crucial roles for particle acceleration in high magnetization cases (Sironi & Spitkovsky

2014; Sironi et al. 2015; Petropoulou et al. 2019). The polarization measurements for reverse shock components may have the potential to identify the acceleration mechanism. The reverse shock radiation also depends on the width of the ejecta. As shown in Figure 13, thin shell cases generate relatively short and bright reverse shock components in optical bands. Such components may be detected as optical flash like GRB 130427A (Vestrand et al. 2014). For thick shell cases, the contribution of both forward and reverse shock components may produce double peak or plateau in optical bands, which can be a key to understanding the multi-wavelength behaviour of the shallow decay phase.

6.2 Onset time and flat light curve in the transition phase

The onset timescale has been theoretically thought to be determined by the traditional deceleration timescale for $\nu > \nu_m$ (for $\nu < \nu_m$, however, a chromatic peak appears at the ν_m crossing timescale) (Kobayashi & Zhang 2007; Ror et al. 2023). The deceleration length scale given by Eq. (9) provides the observed deceleration time as

$$t_{\text{dec}} \simeq (1+z) \frac{R_{\text{dec}}}{2c\Gamma_0^2} \simeq 10^2 \text{ s} (1+z) \left(\frac{E_0}{10^{52} \text{ erg s}^{-1}} \right)^{1/3} \left(\frac{n_0}{1 \text{ cm}^{-3}} \right)^{-1/3} \left(\frac{\Gamma_0}{100} \right)^{-8/3}, \quad (72)$$

where we use typical values for GRB afterglows. As Figure 13 suggests, even for the same R_{dec} , the onset time has diversity within $O(10^1) \sim O(10^3)$ s. For the thin shell case with $\sigma_0 = 10^{-2}$, the onset time is consistent with the conventional estimate. On the other hand, the thin shell with $\sigma_0 = 10$ experiences efficient magnetic acceleration, leading to a shorter onset time due to a larger Lorentz factor than Γ_0 . For the thick shell cases, the peak time is affected by the transition phase. The existence of the transition phase is basically determined by the thickness of the ejecta: $\Delta_0 > R_{\text{dec}}/(\Gamma_0^2 c)$.

The transition phase produces a flatter/rising slope (Mimica et al. 2009; van Eerten 2014) compared to the lightcurve at the coasting phase $F_\nu \propto t_{\text{obs}}^{2-3}$ in the conventional model (Sari & Piran 1999b). Since the transition phase lasts until the rarefaction catch-up time t_{BM} , the thick shell models are preferred to make a long-lasting flat lightcurve as shown in the top panels of Figure 13. The Lorentz factor in the transition phase decreases as $\Gamma_{\text{FS}} \propto t^{-1/2} \propto t_{\text{obs}}^{-1/4}$. Then, we find the time evolution of the observed flux as

$$\nu F_\nu \propto \begin{cases} t_{\text{obs}}^{4/3} & \nu < \nu_m \\ t_{\text{obs}}^{-\frac{p-3}{2}} & \nu_m < \nu < \nu_c \\ t_{\text{obs}}^{-\frac{p-2}{2}} & \nu_c < \nu < \nu_M \end{cases}, \quad (73)$$

for the slow cooling case ($\nu_m < \nu_c$), and

$$\nu F_\nu \propto \begin{cases} t_{\text{obs}}^{4/3} & \nu < \nu_c \\ t_{\text{obs}}^{1/2} & \nu_c < \nu < \nu_m \\ t_{\text{obs}}^{-\frac{p-2}{2}} & \nu_m < \nu < \nu_M \end{cases}, \quad (74)$$

for the fast cooling case ($\nu_c < \nu_m$). A gradual flux evolution $F_\nu \propto t_{\text{obs}}^{1.1}$ in optical bands was observed in GRB 080710A (Krühler et al. 2009a). While this index cannot be explained by standard on and off-axis structured jet scenario (Obayashi et al. 2024), our model expectation $F_\nu \propto t_{\text{obs}}^{4/3}$ is well consistent with it.

Assuming the typical particle spectral index of $p = 2.2$, the transition phase can produce plateau lightcurve for high frequency (slow cooling: $t_{\text{obs}}^{0.4}$, $t_{\text{obs}}^{-0.1}$; fast cooling: $t_{\text{obs}}^{-0.1}$). Such a plateau emission was observed as optical plateau: GRB 050801 (Rykoff et al. 2006), XRF 071031 (Krühler et al. 2009b), GRB 080310 (Littlejohns et al. 2012), GRB 080603A (Guidorzi et al. 2011), and also as enigmatic X-ray shallow decay phase observed in most GRBs (Tang et al. 2019; Zhao et al. 2019) (but not so evident for GeV/TeV-detected GRBs Yamazaki et al. 2020). Our model also expects GeV/TeV plateau emission during the shallow decay phase, which can be tested by future observations.

The end of the shallow decay phase is determined by the rarefaction catch-up times t_{BM} given in Eq. (65), which strongly depends on the initial width of the ejecta. Although the timescale (~ 700 s) corresponds to the shell width in our thick shell model is slightly longer than the typical duration of the prompt emission, the flat lightcurves are consistent with the duration (a few 10^3 s) of the shallow decay phase. Our model is similar to the energy injection model, which requires long-lived central engine activity such as late fallback accretion or new-born magnetar (Zhang & Mészáros 2001; Zhang et al. 2006; Granot & Kumar 2006; Asano 2024); In our case, however, the effective energy injection from the shocked ejecta lasts for a significantly longer timescale than the reverse shock crossing time. We do not need a long reverse shock crossing time close to the shallow decay duration as assumed in Leventis et al. (2014). Furthermore, to reproduce the shallow decay, we do not need to adjust the evolution of the energy injection from the central engine as assumed in the conventional model.

6.3 TeV afterglow in the acceleration phase

Because the acceleration phase is very short for observers, the emission in this phase is difficult to detect. However, if the initial Lorentz factor is small and the width is sufficiently thin, it can be detected at most ~ 10 s. The Lorentz factor in the acceleration phase increases as $\Gamma_{\text{FS}} \propto t^{1/3} \propto t_{\text{obs}}^1$. Then, the observed SSC flux roughly increases as $\nu F_\nu \propto \Gamma^3 R^4 \propto t_{\text{obs}}^{15}$. This index is surprisingly consistent with the recently reported steep rising index of early TeV emission for GRB221009A (LHAASO Collaboration et al. 2023). This could be the first evidence of the magnetic acceleration seen in GRB afterglows.

Since the acceleration phase is at most ~ 10 s, the keV–MeV components are probably overwhelmed by the prompt emission. Since the very high-energy components may experience $\gamma\gamma$ absorption in the prompt phase, the very early TeV afterglows might be important tracers for the acceleration phase. At present, only a few TeV afterglows have been confirmed (MAGIC Collaboration et al. 2019; Abdalla et al. 2019; H. E. S. S. Collaboration et al. 2021; LHAASO Collaboration et al. 2023). We expect the Cherenkov Telescope Array (CTA) will detect a lot of TeV afterglows in the next decade, a part of which may show a steep rise in the TeV band.

7 SUMMARY

In the context of the GRB afterglow, we study the effects of the magnetization of the ejecta on the dynamics and radiation by 1D ideal relativistic MHD simulations for a wide range of the magnetization parameter as $\sigma_0 = 0.01$ –10 and the initial thickness $\Delta_0/R_{\text{dec}} = 0.001$ –0.01. We have confirmed that the magnetic effects can modify the forward and reverse shock dynamics and radiations. From the simulation results, we have constructed analytical formulae of the shock

Lorentz factor evolution, with which we can model the afterglow light curves even for parameter ranges difficult to treat in numerical simulations.

The initial acceleration phase lasts until the reverse shock ignition time. For the magnetized thin shell case, the magnetic field efficiently accelerates the ejecta as $\Gamma \propto t^{1/3}$. Interestingly, this behaviour produces the steep SSC flux evolution $F_\nu \propto t_{\text{obs}}^{15}$, which is similar to the observed early TeV light curve in GRB 221009A.

After the acceleration phase, the Lorentz factor evolution of the forward shock can be divided into three phases – the coasting phase, the transition phase, and the BM phase. The deceleration time t_{dec} is an indicative parameter for the energy equipartition time, but the actual transition to the BM phase occurs later when the rarefaction wave catches up with the forward shock front.

In the transition phase, the deceleration of the forward shock is suppressed by the effective energy injection from the shocked ejecta, resulting in $\Gamma_{\text{FS}} \propto t^{1/2}$. The shock evolution slightly depends on σ_0 in the transition phase. The transition phase in the thick shell case can produce a flat $F_\nu \propto t_{\text{obs}}^{-0.1}$ light curve lasting $10^{3.5}$ s, which is consistent with the observed characteristics of X-ray shallow decay phase. Even with a reasonable thickness of the ejecta, a longer catch-up time of the rarefaction wave than the reverse shock crossing time can reproduce the duration of the shallow decay phase without a fine-tuned engine activity.

The ignition time of the reverse shock emission corresponds to the start of the coasting phase of the forward shock. Until the reverse shock crossing time t_Δ , the Lorentz factor evolution of the reverse shock is almost the same as that of the forward shock. The reverse shock crossing time is well approximated by the analytical expression Eq. (46). The weak energy dissipation by the reverse shock for high σ_0 makes the observed flux lower. The peak time of the reverse shock light curve is regulated by the reverse shock crossing time. As we have demonstrated, the duration and flux of the reverse shock emission depend on the magnetization. The separation of the forward shock and reverse shock components in the lightcurve data could be crucial to determining the magnetization of the ejecta.

Our model in this study will be tested by future observations. An increase of detection for the very rapid rising of TeV afterglow by LHAASO and CTA may provide a hint of the magnetic acceleration of the ejecta. The simultaneous detection of X-rays and GeV γ -rays in the shallow-decay phase with reverse shock components in optical bands will constrain an ejecta width and magnetization, which justifies the existence of our proposed transition phase.

ACKNOWLEDGEMENTS

The authors are grateful to J. Granot for useful comments on the manuscript. The authors thankfully acknowledge the computer resources provided by the Institute for Cosmic Ray Research (ICRR), the University of Tokyo. This work is supported by the joint research program of ICRR, and JSPS KAKENHI Grant Numbers JP23KJ0692 (Y.K.), and JP22K03684, JP23H04899, 24H00025 (K.A.).

DATA AVAILABILITY

The data underlying this article will be shared on reasonable request to the corresponding author.

REFERENCES

- Abdalla H., et al., 2019, *Nature*, **575**, 464
- Aksulu M. D., Wijers R. A. M. J., van Eerten H. J., van der Horst A. J., 2020, *MNRAS*, **497**, 4672
- Asano K., 2024, *ApJ*, **970**, 141
- Asano K., Terasawa T., 2009, *ApJ*, **705**, 1714
- Asano K., Takahara F., Kusunose M., Toma K., Kakuwa J., 2014, *ApJ*, **780**, 64
- Asano K., Murase K., Toma K., 2020, *ApJ*, **905**, 105
- Ayache E. H., van Eerten H. J., Eardley R. W., 2022, *MNRAS*, **510**, 1315
- Bell A. R., 1978, *MNRAS*, **182**, 147
- Berger M. J., Olier J., 1984, *Journal of Computational Physics*, **53**, 484
- Bersier D., et al., 2003, *ApJ*, **583**, L63
- Blandford R. D., McKee C. F., 1976, *Physics of Fluids*, **19**, 1130
- Blandford R. D., Ostriker J. P., 1978, *ApJ*, **221**, L29
- Blandford R. D., Znajek R. L., 1977, *MNRAS*, **179**, 433
- Blumenthal G. R., Gould R. J., 1970, *Reviews of Modern Physics*, **42**, 237
- Chattopadhyay T., et al., 2022, *ApJ*, **936**, 12
- Daigne F., Mochkovitch R., 1998, *MNRAS*, **296**, 275
- Derishev E., Piran T., 2021, *ApJ*, **923**, 135
- Di Gesu L., et al., 2022, *ApJ*, **938**, L7
- Dichiara S., et al., 2022, *MNRAS*, **512**, 2337
- Duffell P. C., Laskar T., 2018, *ApJ*, **865**, 94
- Evans P. A., et al., 2009, *MNRAS*, **397**, 1177
- Fan Y., Piran T., 2006, *MNRAS*, **369**, 197
- Fan Y.-Z., Dai Z.-G., Huang Y.-F., Lu T., 2002, *Chinese J. Astron. Astrophys.*, **2**, 449
- Fan Y.-Z., Piran T., Narayan R., Wei D.-M., 2008, *MNRAS*, **384**, 1483
- Fouka M., Ouichaoui S., 2013, *Research in Astronomy and Astrophysics*, **13**, 680
- Fraija N., Veres P., 2018, *ApJ*, **859**, 70
- Fraija N., Dichiara S., Pedreira A. C. d. E. S., Galvan-Gamez A., Becerra R. L., Barniol Duran R., Zhang B. B., 2019, *ApJ*, **879**, L26
- Fukushima T., To S., Asano K., Fujita Y., 2017, *ApJ*, **844**, 92
- Gao H., Lei W.-H., Zou Y.-C., Wu X.-F., Zhang B., 2013, *New Astron. Rev.*, **57**, 141
- Giannios D., Mimica P., Aloy M. A., 2008, *A&A*, **478**, 747
- Gottlieb S., Shu C. W., 1998, *Mathematics of Computation*, **67**, 73
- Gottlieb O., Moseley S., Ramirez-Aguilar T., Murguía-Berthier A., Liska M., Tchekhovskoy A., 2022, *ApJ*, **933**, L2
- Gould R. J., Schröder G. P., 1967, *Physical Review*, **155**, 1404
- Granot J., 2005, *ApJ*, **631**, 1022
- Granot J., 2012a, *MNRAS*, **421**, 2442
- Granot J., 2012b, *MNRAS*, **421**, 2467
- Granot J., Kumar P., 2006, *MNRAS*, **366**, L13
- Granot J., Komissarov S. S., Spitkovsky A., 2011, *MNRAS*, **411**, 1323
- Guidorzi C., et al., 2011, *MNRAS*, **417**, 2124
- Gupta R., et al., 2021, *MNRAS*, **505**, 4086
- Gupta R., et al., 2022, *MNRAS*, **511**, 1694
- Gupta R., et al., 2024, *ApJ*, **972**, 166
- H. E. S. S. Collaboration et al., 2021, *Science*, **372**, 1081
- Hillas A. M., 1984, *ARA&A*, **22**, 425
- Huang X.-L., Xin L.-P., Yi S.-X., Zhong S.-Q., Qiu Y.-L., Deng J.-S., Wei J.-Y., Liang E.-W., 2016, *ApJ*, **833**, 100
- Japelj J., et al., 2014, *ApJ*, **785**, 84
- Jin Z.-P., et al., 2013, *ApJ*, **774**, 114
- Kennel C. F., Coroniti F. V., 1984, *ApJ*, **283**, 694
- Keshet U., Waxman E., 2005, *Phys. Rev. Lett.*, **94**, 111102
- Kobayashi S., Sari R., 2000, *ApJ*, **542**, 819
- Kobayashi S., Zhang B., 2003, *ApJ*, **582**, L75
- Kobayashi S., Zhang B., 2007, *ApJ*, **655**, 973
- Kobayashi S., Piran T., Sari R., 1997, *ApJ*, **490**, 92
- Komissarov S. S., 2012, *MNRAS*, **422**, 326
- Krühler T., et al., 2009a, *A&A*, **508**, 593
- Krühler T., et al., 2009b, *ApJ*, **697**, 758
- Kurganov A., Tadmor E., 2000, *Journal of Computational Physics*, **160**, 241
- Kusafuka Y., Asano K., Ohmura T., Kawashima T., 2023, *MNRAS*, **526**, 512

- LHAASO Collaboration et al., 2023, *Science*, **380**, 1390
- Laskar T., et al., 2013, *ApJ*, **776**, 119
- Leventis K., Wijers R. A. M. J., van der Horst A. J., 2014, *MNRAS*, **437**, 2448
- Li L., Wu X.-F., Lei W.-H., Dai Z.-G., Liang E.-W., Ryde F., 2018, *ApJS*, **236**, 26
- Liang E.-W., Zhang B.-B., Zhang B., 2007, *ApJ*, **670**, 565
- Liodakis I., et al., 2022, *Nature*, **611**, 677
- Littlejohns O. M., et al., 2012, *MNRAS*, **421**, 2692
- Lyutikov M., 2010, *Phys. Rev. E*, **82**, 056305
- MAGIC Collaboration et al., 2019, *Nature*, **575**, 455
- Mészáros P., Rees M. J., 1997, *ApJ*, **476**, 232
- Mignone A., Bodo G., 2006, *MNRAS*, **368**, 1040
- Mignone A., McKinney J. C., 2007, *MNRAS*, **378**, 1118
- Mignone A., Plewa T., Bodo G., 2005, *ApJS*, **160**, 199
- Mimica P., Aloy M. A., Müller E., Brinkmann W., 2004, *A&A*, **418**, 947
- Mimica P., Giannios D., Aloy M. A., 2009, *A&A*, **494**, 879
- Murase K., 2007, *Phys. Rev. D*, **76**, 123001
- Nakar E., Ando S., Sari R., 2009, *ApJ*, **703**, 675
- Nemmen R. S., Georganopoulos M., Guiriec S., Meyer E. T., Gehrels N., Sambruna R. M., 2012, *Science*, **338**, 1445
- Nousek J. A., et al., 2006, *ApJ*, **642**, 389
- Oates S. R., et al., 2009, *MNRAS*, **395**, 490
- Obayashi K., Toriyama A., Murakoshi M., Sato Y., Tanaka S. J., Sakamoto T., Yamazaki R., 2024, *Journal of High Energy Astrophysics*, **41**, 1
- Panaitecu A., Kumar P., 2004, *MNRAS*, **353**, 511
- Panaitecu A., Mészáros P., Burrows D., Nousek J., Gehrels N., O'Brien P., Willingale R., 2006, *MNRAS*, **369**, 2059
- Perley D. A., et al., 2014, *ApJ*, **781**, 37
- Petropoulou M., Sironi L., Spitkovsky A., Giannios D., 2019, *ApJ*, **880**, 37
- Planck Collaboration et al., 2020, *A&A*, **641**, A6
- Plotnikov I., Grassi A., Grech M., 2018, *MNRAS*, **477**, 5238
- Porth O., et al., 2019, *ApJS*, **243**, 26
- Racusin J. L., et al., 2008, *Nature*, **455**, 183
- Rees M. J., 1978, *MNRAS*, **184**, 61P
- Rees M. J., Meszaros P., 1992, *MNRAS*, **258**, 41
- Rees M. J., Meszaros P., 1994, *ApJ*, **430**, L93
- Ren J., Wang Y., Dai Z.-G., 2024, *ApJ*, **962**, 115
- Rhoads J. E., 1999, *ApJ*, **525**, 737
- Roe P. L., 1986, *Annual Review of Fluid Mechanics*, **18**, 337
- Roming P. W. A., et al., 2006, *ApJ*, **652**, 1416
- Ror A. K., et al., 2023, *ApJ*, **942**, 34
- Rusanov V., 1962, *USSR Computational Mathematics and Mathematical Physics*, **1**, 304
- Ryan G., van Eerten H., Piro L., Troja E., 2020, *ApJ*, **896**, 166
- Rybicki G. B., Lightman A. P., 1986, *Radiative Processes in Astrophysics*. Wiley, New York, NY, doi:10.1002/9783527618170
- Rykoff E. S., et al., 2006, *ApJ*, **638**, L5
- Rykoff E. S., et al., 2009, *ApJ*, **702**, 489
- Sari R., 1997, *ApJ*, **489**, L37
- Sari R., Esin A. A., 2001, *ApJ*, **548**, 787
- Sari R., Piran T., 1995, *ApJ*, **455**, L143
- Sari R., Piran T., 1999a, *ApJ*, **517**, L109
- Sari R., Piran T., 1999b, *ApJ*, **520**, 641
- Sari R., Piran T., Narayan R., 1998, *ApJ*, **497**, L17
- Sari R., Piran T., Halpern J. P., 1999, *ApJ*, **519**, L17
- Shen R., Matzner C. D., 2012, *ApJ*, **744**, 36
- Sironi L., Spitkovsky A., 2011, *ApJ*, **726**, 75
- Sironi L., Spitkovsky A., 2014, *ApJ*, **783**, L21
- Sironi L., Spitkovsky A., Arons J., 2013, *ApJ*, **771**, 54
- Sironi L., Petropoulou M., Giannios D., 2015, *MNRAS*, **450**, 183
- Steele I. A., Mundell C. G., Smith R. J., Kobayashi S., Guidorzi C., 2009, *Nature*, **462**, 767
- Suresh A., Huynh H. T., 1997, *Journal of Computational Physics*, **136**, 83
- Tang C.-H., Huang Y.-F., Geng J.-J., Zhang Z.-B., 2019, *ApJS*, **245**, 1
- Taub A. H., 1948, *Physical Review*, **74**, 328
- Veres P., Duvall W., Goldstein A., Briggs M. S., Grove J. E., 2024, *arXiv e-prints*, p. arXiv:2408.13199
- Vestrand W. T., et al., 2014, *Science*, **343**, 38
- Wang X.-Y., He H.-N., Li Z., Wu X.-F., Dai Z.-G., 2010, *ApJ*, **712**, 1232
- Waxman E., 1997, *ApJ*, **491**, L19
- Wei D. M., Yan T., Fan Y. Z., 2006, *ApJ*, **636**, L69
- Weisskopf M. C., et al., 2022, *Journal of Astronomical Telescopes, Instruments, and Systems*, **8**, 026002
- Wu X. F., Dai Z. G., Huang Y. F., Lu T., 2005, *ApJ*, **619**, 968
- Yamazaki R., Sato Y., Sakamoto T., Serino M., 2020, *MNRAS*, **494**, 5259
- Yang J., et al., 2023, *ApJ*, **947**, L11
- Zhang B., 2018, *The Physics of Gamma-Ray Bursts*, doi:10.1017/9781139226530.
- Zhang B., Kobayashi S., 2005, *ApJ*, **628**, 315
- Zhang B., Mészáros P., 2001, *ApJ*, **552**, L35
- Zhang B., Fan Y. Z., Dyks J., Kobayashi S., Mészáros P., Burrows D. N., Nousek J. A., Gehrels N., 2006, *ApJ*, **642**, 354
- Zhang S., Jin Z.-P., Wei D.-M., 2015, *ApJ*, **798**, 3
- Zhang B., Wang X.-Y., Zheng J.-H., 2024, *Journal of High Energy Astrophysics*, **41**, 42
- Zhao L., Zhang B., Gao H., Lan L., Lü H., Zhang B., 2019, *ApJ*, **883**, 97
- van Eerten H., 2014, *MNRAS*, **442**, 3495
- van Eerten H. J., MacFadyen A. I., 2012, *ApJ*, **751**, 155
- van Eerten H., van der Horst A., MacFadyen A., 2012, *ApJ*, **749**, 44

This paper has been typeset from a $\text{\TeX}/\text{\LaTeX}$ file prepared by the author.